Structural insights into pseudokinase domains of receptor tyrosine kinases

Joshua B. Sheetz[1,2,9], Sebastian Mathea[3,4,5,9], Hanna Karvonen[6,9], Ketan Malhotra[1,2,10], Deep Chatterjee[3,4], Wilhelmiina Niininen[6], Robert Perttilä[6], Franziska Preuss[3,4], Krishna Suresh[7], Steven E. Stayrook[1,2], Yuko Tsutsui[1,2], Ravi Radhakrishnan[7], Daniela Ungureanu[6,8,*], Stefan Knapp[3,4,5,*], and Mark A. Lemmon[1,2,11,*]

[1]Department of Pharmacology, Yale University School of Medicine, New Haven, CT 06520, USA.

[2]Yale Cancer Biology Institute, Yale University West Campus, West Haven, CT 06516, USA.

[3]Institute for Pharmaceutical Chemistry, Johann Wolfgang Goethe-University, D-60438 Frankfurt am Main, Germany

[4]Buchmann Institute for Molecular Life Sciences, Structural Genomics Consortium, D-60438 Frankfurt am Main, Germany

[5]German Cancer Consortium DKTK Frankfurt/Mainz, D-60438 Frankfurt, Germany

[6]Cancer Signaling, Faculty of Medicine and Health Technology and BioMediTech, Tampere University, Tampere, 33014, Finland.

[7]Department of Bioengineering, University of Pennsylvania, Philadelphia, PA 19104, USA.

[8]Genome-Scale Biology, Research Programs Unit, University of Helsinki, FI-00014, Helsinki, Finland

[9]These authors contributed equally

[10]Present address: MRC Laboratory of Molecular Biology, Cambridge Biomedical Campus, Cambridge CB2 0QH, UK.

[11]Lead contact: mark.lemmon@yale.edu

*Correspondence: daniela.ungureanu@tuni.fi (D.U.), knapp@pharmchem.uni-frankfurt.de (S.K.), mark.lemmon@yale.edu (M.A.L.)

Running Title: **RTK pseudokinase structures**

1

SUMMARY

Despite their apparent lack of catalytic activity, pseudokinases are essential signaling molecules. Here, we describe the structural and dynamic properties of pseudokinase domains from the Wnt-binding receptor tyrosine kinases (PTK7, ROR1, ROR2, RYK), which play important roles in development. We determined structures of all pseudokinase domains in this family, and found that they share a conserved inactive conformation in their activation loop that resembles the autoinhibited insulin receptor kinase (IRK). They also have inaccessible ATP binding pockets, occluded by aromatic residues that mimic a cofactor-bound state. Structural comparisons revealed significant domain plasticity, and alternative interactions that substitute for absent conserved motifs. The pseudokinases also showed strikingly similar dynamic properties to IRK. Despite the inaccessible ATP site, screening identified ATP competitive type-II inhibitors for ROR1. Our results set the stage for an emerging therapeutic modality of "conformational disruptors" to inhibit or modulate non-catalytic functions of pseudokinases deregulated in disease.

KEYWORDS
Receptor tyrosine kinases, pseudokinases, Wnt signaling, growth factor signaling, protein conformation, targeted therapies, ponatinib, GZD824, cancer

INTRODUCTION

As receptor tyrosine kinase (RTK) signaling mechanisms have become increasingly well understood (Lemmon and Schlessinger, 2010), those mediated by the subset of RTKs thought to lack kinase activity remain largely enigmatic (Manning et al., 2002; Mendrola et al., 2013). Approximately 10% of the >500 predicted human protein kinases are classed as pseudokinases, assumed to lack phosphotransferase activity because of substitutions of conserved and essential catalytic residues (Boudeau et al., 2006; Manning et al., 2002). Five of the 58 human RTKs fall into this category: ErbB3/HER3, protein tyrosine kinase 7 (PTK7)/colon carcinoma kinase 4 (CCK4), EphB6, EphA10, and SuRTK106 (which lacks an extracellular region and was not included in our study). Three additional RTKs (ROR1, ROR2 and RYK) have substitutions in conserved motifs and lack both kinase activity (Debebe and Rathmell, 2015; Gentile et al., 2011; Katso et al., 1999) and ATP binding (Murphy et al., 2014). These 'RTK pseudokinases' are depicted in Fig. 1A, and the pseudokinase domain sequences are compared in Fig. S1.

Beyond the basic question of how RTKs can signal without kinase activity, strong links of RTK pseudokinases to disease have prompted significant interest in developing therapeutic approaches to inhibit their signaling functions (Bailey et al., 2015; Kung and Jura, 2019). ErbB3 is associated with lung, colon, gastric, and other cancers (Amin et al., 2010; Jaiswal et al., 2013), especially in resistance to inhibitors of other EGFR family members. PTK7, ROR1/2, and RYK are all involved in Wnt signaling (Green et al., 2014; Karvonen et al., 2018; Peradziryi et al., 2012), and elevation of their expression is associated with cancer development and metastasis in several hematological and solid tumors (Debebe and Rathmell, 2015; Karvonen et al., 2018). EphB6 and EphA10 are also reported to play important roles in tumorigenesis (Liang et al., 2019; Nagano et al., 2014). Antibodies targeting the ErbB3 extracellular region are in clinical development for several solid tumors (Jacob et al., 2018). ROR1 antibodies are being tested clinically in chronic lymphocytic leukemia (CLL) and other cancers (Choi et al., 2018;

Choi et al., 2015), as is a small molecule claimed to target the ROR1 extracellular region (Liu et al., 2019). PTK7 is also the target of an antibody-drug conjugate in clinical development (Damelin et al., 2017; Katoh, 2017). No validated pharmacological agents that target intracellular regions of RTK pseudokinases have been described, however – largely because their mechanistic role in signaling is poorly understood.

The nucleotide binding properties of RTK pseudokinase domains vary. Those from PTK7, ROR1/2, and RYK all fail to bind ATP (Murphy et al., 2014), whereas those from ErbB3 and EphB6 bind ATP quite strongly (Jura et al., 2009; Murphy et al., 2014; Shi et al., 2010). ErbB3 also displays low level kinase activity (Shi et al., 2010; Steinkamp et al., 2014), inhibition of which does not block signaling (Novotny et al., 2016; Shi, 2012). Without phosphotransferase activity, pseudokinases are thought to signal by allosterically regulating binding partners (Zeqiraj and van Aalten, 2010). To help understand this role, we combined crystallographic, biophysical, and chemical biology studies. We show that RTK pseudokinase domains adopt structures closely related to the inactive state of their closest kinase-active homologue, and with comparable dynamics – suggesting a similar propensity for conformational changes. We also demonstrate that a pseudokinase domain that fails to bind ATP can nonetheless be targeted with small molecules that bind its vestigial ATP-binding site. The insight provided here into the structure and dynamics of pseudokinase domains suggests approaches for defining the mechanisms of their function and for targeting them pharmacologically.

RESULTS AND DISCUSSION

As a first step, we aimed to establish a comprehensive structural description of RTK pseudokinases – adding to structures of the ErbB3 (Jura et al., 2009; Shi et al., 2010) and ROR2 (Artim et al., 2012) pseudokinase domains. We determined crystal structures of pseudokinases from the remainder of the Wnt-binding RTK (PTK7/ROR/RYK) family, and also modeled the Eph RTK pseudokinases.

The activation loops of PTK7, ROR, and RYK pseudokinase domains mimic autoinhibitory interactions seen in inactive IRK

We determined crystal structures of the PTK7 and RYK pseudokinase domains (to 1.95 Å and 2.38 Å respectively) plus that of ROR1 bound to a small molecule (described in a later section), as summarized in Table 1. These pseudokinase domains all contain a YxxxYY motif (or its vestiges) in the activation loop, similar to that in the insulin receptor kinase domain (IRK). The activation loop conformations also closely resemble that of inactive, autoinhibited, IRK (Fig. 1B) – immediately raising the question as to what activity or property is 'autoinhibited' in the pseudokinases. Inactive IRK is autoinhibited by simultaneous projection of a key tyrosine side chain (Y1162) into the protein substrate-binding site and occlusion of the ATP-binding site by the IRK DFG motif (Hubbard et al., 1994). The PTK7, RYK, and ROR pseudokinases all similarly place a tyrosine in precisely the same location as Y1162 of IRK (Fig. 1B), and the YxxxYY motif configuration (FxxxYH in RYK) is highly conserved. By contrast, the ErbB3 activation loop adopts a different conformation – instead resembling the inactive EGFR kinase domain (Jura et al., 2009; Shi et al., 2010). ErbB3 does place its single activation loop tyrosine (Y848; not conserved in EGFR) in a very similar location to Y1162 in IRK, however (Littlefield et al., 2014), suggesting that projecting an activation loop tyrosine into the (protein) substrate binding site may be common across RTK pseudokinases (Fig. 1C).

The ATP-binding site of inactive IRK is occluded in two ways (Hubbard et al., 1994). First, the side-chain of the DFG phenylalanine (F1151) projects into the adenine ring binding site (Fig. 1D: IRK inactive). Second, the main chain following the DFG motif occludes the binding site for the ATP β- and γ-phosphate groups (Fig. 1D). This is the 'DFG-out' conformation (Huse and Kuriyan, 2002; Modi and Dunbrack, 2019), frequently seen in inactive kinases – in which the aspartate side-chain (D1150) is also oriented away from the active site so that is cannot coordinate Mg^{2+}. In active kinases, the DFG motif instead adopts an 'in' conformation,

allowing Mg^{2+} coordination and repositioning the phenylalanine side-chain to allow ATP binding

and to complete the so-called regulatory spine (Fig. S2) or 'R-spine' (Kornev and Taylor, 2010).

The Wnt-binding RTK pseudokinases all have an altered DFG motif ('ALG' in PTK7, 'DLG' in the

RORs and 'DNA' in RYK; Fig. 1D). The conformation of this altered motif is always closer to

'DFG-out' than 'DFG-in' (Fig. 1D). As a result, each R-spine is broken (Fig. S2) – although in a

different way for RYK than for PTK7 or ROR2 (which more closely resemble inactive IRK).

Moreover, the leucine side-chains in the PTK7 'ALG' motif (L949) and the ROR2 'DLG' motif

(L634) occlude the ATP-binding site (Fig. 1D). RYK is an exception, as its 'DNA' motif lacks a

corresponding hydrophobic side-chain – although the main chain after this motif passes through

(and occludes) the β/γ phosphate group-binding region (Fig. 1D). In contrast with the Wnt

pseudokinase RTKs, the ErbB3 DFG motif adopts an 'in' conformation that completes the R-

spine and leaves the ATP-binding site open to allow nucleotide binding (Figs. 1D and S2).

Aromatic side-chains from the hinge region occlude the PTK7, ROR, and RYK ATP-binding sites

ATP binding to PTK7 and ROR2 is prevented by projection of a tyrosine side-chain from the

β5/αD hinge region (Y877 and Y555 respectively) into the adenine ring binding site (Fig. 1D).

This position is two residues C-terminal to the gatekeeper, and is a tyrosine in ~50% of tyrosine

kinases – although replaced by leucine (L1078) in IRK. The side-chain at this position typically

projects away from the ATP binding site (as for L1078 in IRK and Y770 in ErbB3; Fig. 1D). The

alternative side-chain orientation in PTK7 and ROR2 results from a rotation of their N-lobes

about the β5/αD hinge (Fig. S3A,B). RYK does not undergo this N-lobe rotation (Fig. S3C),

allowing its corresponding tyrosine (Y413) to adopt the canonical orientation (Fig. 1D). The RYK

adenine ring binding site is instead occluded by the side-chain of a phenylalanine (F362) in the

altered $\beta3$ VAIK motif (AFVK in RYK). A leucine at this position in PTK7 (L828 in its VLVK

variant of the VAIK motif) also contributes to ATP-binding site occlusion.

Whereas the ATP binding sites in RTK pseudokinases are occluded by side-chains from

multiple motifs, the IRK ATP-binding site is only obstructed by its DFG motif (Figs. 1D and S4A),

suggesting that simply flipping the DFG motif from 'out' to 'in' might allow ATP binding. Indeed,

IRK can bind Mg^{2+}-ATP without activation loop phosphorylation (Till et al., 2001) as can be seen

using differential scanning fluorimetry (DSF). DSF monitors the influence of ligand binding on

the melting temperature (T_M) of a protein, as reported by increased fluorescence of SYPRO

Orange as it binds to thermally unfolded protein (Fedorov et al., 2012). Binding of Mg^{2+}-ATP to

unphosphorylated IRK destabilized the kinase domain by ~3.5˚C (Fig. S4B) – rather than

stabilizing – which may reflect disruption of the autoinhibitory activation loop interactions

described above. In contrast to IRK, the PTK7, ROR1, ROR2, and RYK pseudokinase domains

showed no significant stability change upon adding 5 mM Mg^{2+}-ATP (Fig. S4B), suggesting no

binding, in agreement with previous work (Murphy et al., 2014). Moreover, a D644A mutation in

ROR2 (equivalent to D1161A in IRK, which promotes ATP binding) failed to restore ATP

binding.

Another important difference between IRK and the Wnt-binding RTK pseudokinases is

revealed by comparing their catalytic spines ('C-spines'). The 'C-spine' is a non-contiguous

hydrophobic motif defined by Kornev and Taylor (Kornev and Taylor, 2010). In ATP-bound

active kinases, it is completed by the adenine ring of bound ATP, as seen in PKA and active

IRK in Fig. S2. In an inactive kinase, by contrast, the C-spine is broken (see inactive IRK in Fig.

S2) and the side-chain of the DFG-motif phenylalanine (from the R-spine) projects into the gap.

Interestingly, the C-spine is fully contiguous in PTK7, ROR2 and RYK despite no direct

contribution from R-spine (DFG motif) residues or ATP (Fig. S2) – although the side-chain of the

ALG/DLG motif leucine does abut the intact C-spine in PTK7 and ROR2.

PTK7, ROR, and RYK pseudokinases adopt different 'hybrid' conformations stabilized by unique sets of interactions

Although the PTK7, ROR, and RYK pseudokinase domains all closely resemble inactive IRK in their activation loop configurations (Fig. 1B), they vary substantially in αC helix position (Fig. 2A) and in other structural features, details of which can be described as follows.

PTK7: Although PTK7 appears autoinhibited by its activation loop (and hinge tyrosine), it has an active-like 'in' αC disposition (Fig. 2A). As a result, the distance between the side-chains of the conserved αC glutamate (E846) and the VAIK motif β3 lysine (K830) is just 2.7 Å. This allows the αC/β3 salt bridge – a hallmark of active kinases – to form (Fig. 2B), and places K830 so that it could support ATP binding if the ATP-binding site were not occluded. PTK7 thus adopts an unusual 'pseudo' active-like kinase domain conformation.

ROR2: The ROR2 αC helix adopts the 'out' position as in inactive IRK (Fig. 2A). The side-chains of the αC glutamate (E524) and β3 lysine (K507) are therefore too far apart (~5 Å) for the hallmark αC/β3 salt bridge of active kinases to form (Fig. 2C) – and the β3 lysine (K507) is >7 Å away from where the ATP phosphates would reside in a putative nucleotide-bound state (Artim et al., 2012). A hydrogen bond between D633 in the degenerated ROR2 DFG motif (DLG) and R528 in αC also connects these two motifs in an unusual way (Fig. 2C).

RYK: The RYK pseudokinase domain has several unique structural features. First, as in PTK7, its αC helix adopts an _active_-like 'in' position (Fig. 2A), apparently 'pushed' into this position by a 2.5-turn α-helix (αB) at the domain's amino-terminus (Fig. 2D). This arrangement is reminiscent of the EphB2 kinase domain (Wybenga-Groot et al., 2001) and involves intimate clustering of hydrophobic side-chains at the αB/αC interface (Fig. 2D, left). Surprisingly, although the conserved β3 lysine (K364) is retained in RYK's degenerated VAIK motif (AFVK), and αC is 'in', the αC/β3 salt bridge that is a hallmark of active kinases does not form in RYK (Fig. 2D, right). Instead, K364 forms a predicted salt-bridge (2.6 Å) with D483 in RYK's

degenerated DFG (DNA) motif, and the αC glutamate (E381) is close (3.0 Å) to R488 in the activation loop (three residues C-terminal to the degenerated DFG motif). The absence of a large hydrophobic side-chain in RYK's degenerated DFG motif also appears to be compensated for by the positioning of F491 in the small helix C-terminal to this motif (Fig. S4A). In addition, the presence of a glutamine (Q337) in place of the first glycine of the glycine rich loop in RYK contributes to steric exclusion of RYK's ATP binding site (Fig. S4A).

Differences in Eph pseudokinase domain autoinhibition

To extend these comparisons across the RTK pseudokinases, we modeled the EphA10 and EphB6 pseudokinase domains, so far of unknown structure. Apart from EphA10 and EphB6, the remaining 12 human ephrin receptors (Ephs) are catalytically active (Liang et al., 2019). They are regulated by phosphorylation of key juxtamembrane (JM) tyrosines, which relieves intramolecular autoinhibition to allow *trans*-autophosphorylation of a conserved activation loop tyrosine (Hornbeck et al., 2015) that corresponds to Y1162 in IRK. EphA10 retains this conserved activation loop tyrosine, but not the regulatory JM tyrosines. Conversely, EphB6 retains the regulatory JM tyrosines but not the activation loop tyrosine (and has an unusually short activation loop). In the few published Eph kinase structures in inactive conformations (Dong et al., 2014; Kung et al., 2016; Overman et al., 2014), the activation loop tyrosine is ordered and projects into the substrate binding site like Y1162 of inactive IRK. Similarly, our EphA10 pseudokinase model, (based on EphB3; see STAR Methods) places this tyrosine (Y801) in the autoinhibitory location (Fig. 3A,B). Y801 simultaneously contacts the arginine close to the end of the catalytic loop (R774 in EphA10) and an adjacent EphA10-specific histidine (H775) – substituting for interaction with the (absent) HRD aspartate (Fig. 3B). This IRK-like docking of Y801 constrains the EphA10 activation loop so that the backbone of the DFG motif (GFG in EphA10) passes through and occludes the ATP-binding site as in IRK (Fig.

9

3C). No additional occlusion of the ATP-binding site from the β5/αD hinge is seen, suggesting

that EphA10 shares IRK's ATP-binding properties.

EphB6 lacks 14 activation loop residues (including the conserved tyrosine), so cannot

adopt the inactive-like conformation seen in IRK and EphA10. Instead, the shortened and

unrestrained EphB6 activation loop adopts an active-like conformation in our models (Fig. 3),

leaving EphB6 free to bind ATP as reported experimentally (Becher et al., 2013; Murphy et al.,

2014) – with a possible positive contribution from R813 (Fig. 3C). Thus, whereas EphA10

seems to resemble IRK and the Wnt-binding RTK pseudokinases, EphB6 appears to resemble

ErbB3 in having an unprotected ATP-binding site.

Pseudokinases and kinases display similar conformational dynamics

It has been hypothesized that pseudokinases function as allosteric regulators or scaffolding

molecules in cell signaling (Kung and Jura, 2019; Reiterer et al., 2014; Zeqiraj and van Aalten,

2010), which might require dynamic transitions between different conformational states as seen

for canonical kinases (Huse and Kuriyan, 2002; Kornev and Taylor, 2015). Alternatively,

pseudokinase domains might be more static than other kinase domains, allowing them to serve

as rigid scaffolds – a view suggested by the fully occluded ATP-binding sites, well-defined

autoinhibitory activation loops, and additional intramolecular interactions seen in PTK7, ROR2

and RYK but not in other protein kinases. To distinguish between these possibilities, we used

hydrogen-deuterium exchange coupled with mass spectrometry (HDX-MS) to compare

exchange dynamics of the pseudokinase domains with those of unphosphorylated, inactive IRK.

IRK activation requires the unphosphorylated activation loop to explore multiple

conformations. These fluctuations can transiently reverse autoinhibition so that Mg^{2+}-ATP and

substrate tyrosine can bind (Hubbard, 2013) – and the kinase can *trans*-phosphorylate its

neighbor in an insulin receptor dimer to promote signaling. HDX-MS studies of IRK (Fig. 4A)

illustrate this dynamic conformational exploration, with backbone amide protons in the YxxxYY

motif-containing activation loop becoming almost completely exchanged within ~1 minute. Other

regions of IRK are also quite dynamic, whereas the HRD motif (which harbors the catalytic base

aspartate) and the $\beta5/\alpha D$ hinge (between N- and C-lobes) show the slowest HDX rates (Fig.

4A,B; Table S1). A similar overall dynamic picture has been reported for other protein kinases

studied by HDX-MS (Bunney et al., 2018; Hsu et al., 2008; Iacob et al., 2009; Loving and

Underbakke, 2019; Shi et al., 2006; Sours et al., 2008; Tsutsui et al., 2016), so IRK appears

typical.

Far from being more static than typical kinases, all of the pseudokinase domains studied

here show very similar dynamic characteristics to IRK (Fig. 4C). Most importantly, the activation

loops of the pseudokinase domains – which contain the DFG and YxxxYY motifs – all showed

very similar HDX rates to those of IRK. The pseudokinases also share with IRK a relatively low

rate of exchange in the HRD motif. Other general trends are also similar, although each

pseudokinase does display some unique features, such as increased $\beta2/\beta3$ loop exchange in

PTK7 and ROR2, and reduced exchange in αC peptides for all pseudokinases compared with

IRK. Regions in the C-lobe (notably αF and beyond) show much more variability from domain to

domain, likely owing to differences in helix and loop lengths. In Fig. 4D, differences between a

mean 'exchangeability index' for the pseudokinase domains as a group (see STAR Methods)

and HDX measured for IRK are plotted on the IRK structure. For most of the structure, the

difference is within two standard deviations of the mean for pseudokinases (white). Differences

exceed 2σ only in αC and the glycine-rich ($\beta1/\beta2$) loop – which both show slightly less exchange

in the pseudokinases (colored darker grey). By contrast, the $\beta5/\alpha D$ loop (leading into αD) and

helix αI both show slightly higher exchange in pseudokinases (colored orange).

These results demonstrate that structural elements in the RTK pseudokinase domains

are not significantly more rigid than in catalytically active counterparts such as IRK. This in turn

suggests that the pseudokinases may maintain conformational switching-based regulatory mechanisms seen with active kinases, which could control scaffolding functions in signaling.

The intracellular pseudokinase domain elicits signaling functions

A major challenge in studying the Wnt-binding RTK pseudokinases has been the availability of experimental contexts for structure/function analysis of signaling (Green et al., 2014; Karvonen et al., 2018). Moreover, some in vivo studies have led to inferences that the intracellular pseudokinase domains of Wnt-binding RTKs are not required for signaling (Green et al., 2014; Hayes et al., 2013; Inoue et al., 2004; Stricker et al., 2017) – although this likely reflects Wnt sequestration by the extracellular regions of the overexpressed constructs.

Using an approach frequently employed in studies of RTKs (Collins et al., 1988; Warmuth et al., 2007), we expressed ROR1, ROR2 and PTK7 in the interleukin-3 (IL3) dependent BaF3 murine pro-B cell line (Fig. S5A). Whereas parental BaF3 cells die following IL3 withdrawal, a significant number of those expressing ROR2 survived in the absence of IL3 (Fig. S5B), and those expressing PTK7 showed some improved survival, consistent with previous studies (Prebet et al., 2010). In addition, ROR1-expressing cells (Fig. 5A) ultimately achieved IL3 independent proliferation (Fig. 5B) – consistent with the contribution of ROR1 (but not ROR2) to CLL and other hematological malignancies (Daneshmanesh et al., 2013; Karvonen et al., 2018). Intriguingly, the ROR1-expressing cells also responded to Wnt5a stimulation with significant elevation of ERK, AKT, and SRC phosphorylation (Fig. 5C), whereas no such response was seen in parental BaF3 cells or with ROR2 (Fig. S5C). These findings are consistent with studies of ROR1 signaling in a lymphoblastic leukemia cell-line (Bicocca et al., 2012) as well as other reports (Karvonen et al., 2019; Yamaguchi et al., 2012; Zhang et al., 2019). To ask whether the intracellular pseudokinase domain of ROR1 is required for these responses, we expressed a form of ROR1 that lacks its entire intracellular region (ROR1ΔICR). Despite strong expression (Fig. 5A), ROR1ΔICR lacked the ability to promote IL3-independent

proliferation of BaF3 cells or to support Wnt5a-induced ERK, AKT, and SRC activation (Fig. 5B,C). Mutating the YxxxYY motif in the ROR1 activation loop to FxxxFF also abolished the ability of ROR1 to support BaF3 cell proliferation, as did mutating the VAIK β3 lysine (K506) to alanine (Fig. 5D,E). These data argue that the intracellular region of ROR1 (and those of other RTK pseudokinases) can provide important signaling functions despite lacking phosphotransferase activity. We were unable to detect any residual kinase activity for ROR1 (Fig. S5D,E) – as also reported by others (Murphy et al., 2014). We therefore suggest that the mutations analyzed in Fig. 5 impair ROR1 signaling function by altering the conformation of its pseudokinase domain. Given the status of ROR1 and the other RTK pseudokinases as therapeutic targets, these findings prompted us to investigate targeting them with small molecules that might similarly modulate conformation. Our goal is to identify small molecules that modulate the scaffolding and/or allosteric functions of pseudokinase domains by inducing conformational changes – following precedents set with the TYK2 (Wrobleski et al., 2019), STRAD (Zeqiraj et al., 2009) and KSR (Dhawan et al., 2016) pseudokinases, as well as catalytically active kinases such as Aurora A (Gustafson et al., 2014).

Selective small molecule binders of the ROR1 pseudokinase domain

To identify small molecules that bind the ROR1, ROR2, PTK7, and RYK pseudokinase domains, we again used DSF, screening a total of 1486 compounds from the published protein kinase inhibitor set and the FDA-approved drug set from Selleckchem (see Table S2). The cut-off value for identifying 'hits' was thermal stabilization of ±2˚C (Fig. 6A). Despite the relatively large and kinase inhibitor-focused screening set, we failed to identify any hits for PTK7, ROR2, or RYK. For ROR1, however, we identified two closely related inhibitors that significantly increased T_M – indicating strong binding. These were ponatinib (O'Hare et al., 2009), a multi-targeted kinase inhibitor approved by the FDA for chronic myeloid leukemia (CML) and Philadelphia chromosome-positive acute lymphoblastic leukemia (ALL), and GZD824 (Ren et

al., 2013) – which is structurally related. Both are BCR-ABL inhibitors that retain the ability to inhibit T315I gatekeeper-mutated ABL. Ponatinib and GZD824 stabilized ROR1 by 4.1°C and 6.0°C respectively (Fig. 6A), but did not bind ROR2, RYK, or PTK7. The two inhibitors are typical type-II inhibitors that likely induce a particular DFG-out conformation. The compact nature of their alkyne linker (Fig. 6B) is key for binding to T315I-mutated ABL (it is interesting to note that ROR1 has a phenylalanine at the gatekeeper position). To validate ponatinib and GZD824 as 'hits', and to exclude the possibility that they simply interfere in the DSF assay, we measured T_M for the ROR1 pseudokinase domain at a series of GZD824 concentrations (Fig. 6C). The resulting curve showed clear saturation (at ~10 μM) and an IC_{50} value of ~1 μM (for a ROR1 concentration of 2 μM in the assay) – arguing that K_D is submicromolar. Using a cellular thermal shift assay or CETSA (Martinez Molina et al., 2013), we further showed that both ponatinib and GZD824 engage (and stabilize) full-length ROR1 in BaF3 cells when added at 10 μM (Fig. 6D,E). Maximum stabilization of ROR1 in these assays was achieved with ~2 μM GZD824 or ~5 μM ponatinib (Fig. S6). These data suggest that both inhibitors form stoichiometric complexes with ROR1. Moreover, the fact that neither compound binds detectably to the ROR2, PTK7, or RYK pseudokinase domains demonstrates clear selectivity within the Wnt pseudokinase family – although GZD824 and ponatinib are known to inhibit a range of other tyrosine kinases. Importantly, as discussed below, ROR1-dependent activation of ERK and AKT phosphorylation by Wnt5a is inhibited at the same concentrations of ponatinib and GZD824 that maximally stabilize ROR1 in cells.

Binding of ponatinib or GZD824 induces conformational changes in the ROR1 pseudokinase domain

To investigate whether binding of ponatinib or GZD824 to the ROR1 pseudokinase domain induces conformational changes, we again turned to HDX-MS. Adding excess ponatinib or

GZD824 to the ROR1 pseudokinase domain led to significant protection from exchange in peptides close to the putative ATP-binding site (Fig. 7A,B and Fig. S7A,B), demonstrating that the occluded ATP-binding site of ROR1 can still accommodate kinase inhibitor-like molecules (presumably with associated conformational changes). Binding of ponatinib or GZD824 caused significant HDX protection in helix αC, αE, the β5/αD hinge region, the HRD motif, and the DFG (DLG) motif at the beginning of the activation loop – all regions adjacent to the vestigial ATP-binding site. By contrast, several more remote peptides showed *increased* backbone amide exchange upon inhibitor binding (red in Figs. 7A and S7A,B), arguing that the inhibitors induce significant changes in the pseudokinase domain's conformation. Regions affected in this way (red bars in Fig. 7A) included peptides in the β1/β2 (glycine-rich) loop region, part of strand β3, and much of the ROR1 activation loop – where inhibitor binding increases HDX in an already quite dynamic region of ROR1 (e.g. Fig. 7B, peptide ***iv***), arguing that it destabilizes autoinhibitory interactions.

Crystal structure of the ROR1 pseudokinase domain bound to ponatinib

To directly visualize the mode of inhibitor binding to this pseudokinase, we co-crystallized the ROR1 pseudokinase domain with ponatinib and determined a 1.94 Å crystal structure (Fig. 7C). The structure confirmed that ponatinib binds to the region corresponding to ROR1's ATP-binding site, contacting all of the sites protected in HDX studies. Ponatinib binds ROR1 with the same binding mode seen when it binds ABL (O'Hare et al., 2009), as shown in Fig. S7C. The narrow alkyne linker of ponatinib, key for allowing it to bind T315I-mutated ABL, abuts the bulky gatekeeper phenylalanine (F552) side-chain in ROR1 (Fig. 7C inset). The structure of the ponatinib-bound ROR1 pseudokinase domain is very similar to that for ROR2 (which does not bind ponatinib or GZD824 yet shares 68% sequence identity). The configuration of the ROR1 activation loop YxxxYY motif closely resembles that of ROR2, RYK, PTK7 and inactive IRK in

the static crystallographic view, but our HDX data (Fig. 7A,B) argue that binding of ponatinib or GZD824 significantly increases its solvent accessibility and dynamics. Moreover, the C-terminal part of the activation loop – immediately following the YxxxYY motif – was disordered in the ROR1/ponatinib complex structure, suggesting that accommodating ponatinib partly disrupts autoinhibitory docking of the activation loop in this region.

Another ponatinib-induced conformational change is seen in the DFG motif (DLG in ROR1/2). Ponatinib restrains this motif in ROR1 so that the leucine side-chain is disordered and the DLG aspartate (D633) side-chain is displaced (by ponatinib's trifluoromethylphenyl group) towards H613 of the HRD motif (see Fig. 7C inset). This forces ROR1's DLG motif into the same conformation seen for the DFG motif in ponatinib-bound ABL (O'Hare et al., 2009) – typical of that in kinases bound to type-II inhibitors (Modi and Dunbrack, 2019).

The largest-scale difference between the structures of the ROR1/ponatinib complex and ROR2 (which does not bind ponatinib) is a rotation (~20˚) of the entire N-lobe about an axis (yellow rod in Fig. 7D) nearly coincident with strand β4. Ponatinib appears to simultaneously 'push' on the left-hand side of the N-lobe (near β1 and the β5/αD hinge) and 'pull' on its right-hand side (near αC) to achieve this rotation. Ponatinib displaces the side-chain of the β5/αD hinge tyrosine (Y554 in ROR1, Y555 in ROR2) that occludes ROR2's ATP-binding site, as indicated by the red arrow on the left of Fig. 7D – inserting its imidazo(1,2-b)pyridazine moiety into that pocket. At the same time, ponatinib (docked onto the C-lobe) associates intimately with helix αC of ROR1, through an interaction between the nitrogen of its amide linker and E523 in αC plus van der Waal's contacts with the (hydrophobic) side-chains of L526, M527, and L530 in αC. All the corresponding residues are solvent-exposed in ROR2 (E524, L527, R528, and L531). Importantly, an arginine at position 528 of ROR2 (replaced by M527 in ROR1 – which contacts ponatinib) likely explains why ponatinib binds only ROR1, and not ROR2. An arginine in this position would interfere with ponatinib/αC interactions.

Together with our HDX-MS studies, this comparison of the ponatinib-bound ROR1 and unliganded ROR2 pseudokinase domain structures reveals one way in which a kinase inhibitor-like small molecule binder can modulate the conformation of a pseudokinase domain. Many effectors and activators bind to the N-lobe region of other kinases that is the focus of the conformational changes described here (Jura et al., 2011). Any similar mode of interaction that ROR1 participates in will thus be significantly affected by ponatinib or GZD824 binding. Ponatinib and GZD824 may therefore serve as pharmacologically privileged potential starting points for developing selective small molecule ROR1 interactors that could induce sufficiently extensive conformational changes in the pseudokinase domain to impair scaffolding functions of ROR1 in disease. Although efforts to investigate the effects of these inhibitors on the ROR1-mediated signaling seen in Fig. 5C are currently confounded by the promiscuity of ponatinib and GZD824 as kinase inhibitors, both compounds clearly inhibit ROR1-dependent activation of ERK and AKT phosphorylation by Wnt5a (Fig. S7D) at concentrations that we know maximally stabilize the receptor in CETSA experiments (Fig. S6). Moreover, it is interesting to note that Bicocca et al. found that ponatinib robustly inhibits AKT phosphorylation in acute lymphoblastic leukemia cells (Bicocca et al., 2012), in which ROR1 also appears to signal to AKT and ERK.

CONCLUSIONS

Our structural and modeling studies argue that the inactive kinase domains of RTK pseudokinases nonetheless retain the autoinhibitory interactions seen in their kinase-active relatives – the Wnt-binding RTKs sharing that autoinhibitory YxxxYY activation loop motif conformation seen in inactive IRK. RTK pseudokinases all seem either to bind nucleotide (as in ErbB3 and EphB6) or to mimic an ATP-bound form (as in PTK7, ROR1/2 and RYK) – as reported for others (Hammaren et al., 2015; Scheeff et al., 2009). Which of these two classes they fall into appears to correlate with whether or not the ATP-binding site is occluded in the inactive conformation of their closest kinase-active homologues.

One important question that arises from our results is why the pseudokinases retain the autoinhibitory interactions seen in their kinase-active relatives. One hypothesis is that pseudokinase domains function as rigid scaffolds, and the autoinhibitory interactions could promote rigidity (Kornev and Taylor, 2009; Murphy et al., 2014; Patel et al., 2017; Scheeff et al., 2009). On the contrary, our HDX-MS data argue that the PTK7, ROR, and RYK pseudokinase domains all display similar conformational dynamics to IRK, despite mimicking an ATP-bound state. It is well known that canonical protein kinases such as IRK undergo transitions between active and (family-specific) inactive conformations (Huse and Kuriyan, 2002). The RTK pseudokinases are likely to have similar capabilities, providing a possible mechanism for controlling their ability to interact with binding partners and thus regulate signaling (Jacobsen and Murphy, 2017; Kung and Jura, 2019). In IRK, the inactive-to-active conformational transition is promoted by tyrosine phosphorylation of the activation loop YxxxYY motif (Hubbard, 2013). YxxxYY motif tyrosine phosphorylation has been reported for both PTK7 and ROR2 (Hornbeck et al., 2015), and could promote structural changes similar to those seen in IRK activation. Indeed, phosphorylation of the ROR1 and ROR2 pseudokinase domains has been suggested to be mediated by SRC recruitment (Akbarzadeh et al., 2008; Gentile et al., 2014). A related phosphorylation-dependent mechanism has also been described for the pseudokinase MLKL (mixed lineage kinase domain-like protein), where phosphorylation of the pseudokinase domain induces conformational changes, which control intra- and intermolecular interactions that regulate necroptosis (Petrie et al., 2019). Thus, pseudokinases may not only be scaffolds that allosterically regulate active kinases, but may in fact be regulated as conformational switches.

As with catalytically competent kinases, the dynamic structural changes involved in pseudokinase function might also be modulated by small molecules that bind the ATP site and modulate inter- and/or intra-molecular interactions. It might be possible to exploit this therapeutically. Several small molecules that bind the ATP-binding site of pseudokinases have been reported (Dhawan et al., 2016; Kung and Jura, 2019). For example, BMS-986165, an

ATP-competitive inhibitor that binds the pseudokinase domain of TYK2 (a JAK family member) is effective in several murine models of autoimmune disease and is now in clinical testing (Wrobleski et al., 2019). JAK pseudokinase domains play important roles in regulating activity of their adjacent catalytically-competent (JH1) kinase domains, highlighted by frequent patient-derived JAK-activating mutations in the pseudokinase domain (Shan et al., 2014). In the case of TYK2, the unusual ATP site of its pseudokinase domain allowed selective inhibitor design that resulted in outstanding JAK isoform and kinome selectivity for BMS-986165 (Moslin et al., 2019; Wrobleski et al., 2019). Our findings support the value of similar concerted efforts to find small molecule modulators of the pseudokinase RTKs. Even if modulation of the properties of the pseudokinase domain by small molecules proves insufficient to block pseudokinase function, the ligands developed for the ATP-binding site of these proteins could instead be used for developing proteolysis targeting chimeras (PROTACs), as reported for both kinase-active RTKs (Burslem et al., 2018) and the RTK pseudokinase ErbB3 (Xie et al., 2014).

In conclusion, the results presented here demonstrate the feasibility of targeting the apparently inaccessible ATP site of ROR1 and related RTK pseudokinases. Given the important role of ROR1 and the other Wnt-binding RTKs in mediating growth signals, their selective targeting in this way represents a potentially valuable strategy for the development of future therapeutic agents.

STAR★METHODS

Detailed methods are provided in the online version of this paper and include the following:

- **KEY RESOURCES TABLE**

- **RESOURCE AVAILABILITY**

  - Lead contact for reagent and resource sharing

  - Materials availability

  - Data and code availability

- **EXPERIMENTAL MODEL DETAILS**

  - Cell culture

- **METHOD DETAILS**

  - Plasmid construction for recombinant protein expression

  - Protein production and purification

  - Crystallization

  - Structure determination

  - Hydrogen-deuterium exchange-mass spectrometry (HDX-MS)

  - Differential scanning fluorimetry (DSF)

  - Small molecule screening

  - Homology models of EphA10 and EphB6

  - BaF3 cell transfections

  - Cell viability and cell proliferation

  - Western blotting

  - Cellular thermal shift assays (CETSA)

  - in vitro kinase assays

- **QUANTIFICATION AND STATISTICAL ANALYSIS**

  - Structure determination and analysis

- o   Analysis of HDX dynamics

- o   Western blot image processing

- o   Cell proliferation assays

- o   Cellular thermal shift assays (CETSA)

- **DATA AND SOFTWARE AVAILABILITY**

SUPPLEMENTAL INFORMATION

Supplemental information includes seven figures and two tables, and can be found in the online version of this article.

ACKNOWLEDGMENTS

21

AUTHOR CONTRIBUTIONS

J.B.S., D.U., S.M., K.M., S.K. and M.A.L designed the overall project and wrote the manuscript. J.B.S., S.M., K.M., S.K., and M.A.L. analyzed structures and generated structure figures. K.M., S.M., and S.E.S. carried out crystallographic structural studies, and J.B.S. and Y.T. performed HDX-MS. D.C., F.P., and J.B.S. performed DSF and other biochemical studies, H.K., R.P., W.N. and D.U. performed all cellular and CETSA studies, and K.S and R.R. carried out molecular modeling studies. All authors contributed to analysis of results and editing of the manuscript.

DECLARATION OF INTERESTS

The authors declare no competing interests.

LEGENDS TO FIGURES

FIGURE 1

Pseudokinases retain autoinhibitory interactions of the insulin receptor

(**A**) Domain composition of human RTK pseudokinases, with the extracellular region above, and intracellular region below the membrane. Domains are listed in the legend: pseudokinase (red), leucine-rich (L), cysteine-rich (Cys Rich), immunoglobulin (Ig), Frizzled cysteine-rich domain (Fz CRD), Kringle domain (Kr), Sterile Alpha Motif (SAM), and Wnt Inhibitory Factor (WIF) domain.

(**B**) Activation loops of pseudokinase domains from PTK7 (slate blue), ROR2 (magenta), and RYK (green) are superimposed on that of IRK (black) in the context of the IRK surface (from PDB: 1IRK). YxxxYY tyrosines in IRK are labeled. The ROR2 structure is chain B of PDB: 3ZZW.

(**C**) ErbB3 activation loop structure (Littlefield et al., 2014) from PDB: 4RIW, superimposed on the 1IRK surface as in (**B**), with ErbB3 colored orange. Y849 is labelled.

(**D**) Close-up of residues surrounding the ATP binding site for active and inactive IRK (black), PTK7, ROR2, RYK, and ErbB3, colored as above. AMP-PNP is solid when seen in the relevant crystal structure and transparent when not. Residues from the DFG motif (and 4 residues beyond), the β5/αD hinge, and second residue of the VAIK motif are shown (VAVK in IRK, VLVK in PTK7, VAIK in ROR2, AFVK in RYK, VCIK in ErbB3).

See also Figure S1 and Table 1.

FIGURE 2

Overall structure of pseudokinase domains

(**A**) Cartoon representing pseudokinase αC helix positions. Two orthogonal views of inactive IRK (1IRK) are shown in grey. Helix αC of IRK, which adopts the 'out' position is colored black.

Helix αC from ROR2 (3ZZW; magenta) and ErbB3 (4RIW; orange) is also 'out'. By contrast, αC is 'in' for PTK7 (slate blue), RYK (green), and active IRK (1IR3).

(**B**) PTK7 pseudokinase domain. The insert shows the predicted salt bridge between the αC glutamate (E846) and β3 lysine (K830).

(**C**) ROR2 pseudokinase domain (chain B from 3ZZW). Insert shows absence of salt bridge between the αC glutamate (E524) and β3 lysine (K507), and alternate contact between D633 (in the DLG motif) and R528 (in αC).

(**D**) RYK pseudokinase domain. Inserts show hydrophobic side-chains involved in packing between helices αB and αC (left) and connections between the DFG (DNA) motif region and helix αC (right). Interactions between D483 (in DNA motif) and the β3 lysine (K364) and between R488 (close to DNA motif) and αC glutamate (E381) are shown.

Vestigial ATP-binding sites are labelled in inserts of (**B-D**) using a transparent AMP-PNP molecule positioned as in active IRK.

See also Figure S2.

FIGURE 3

Insights into EphA10 and EphB6 pseudokinases from modeling

(**A**) Activation loops in models of the EphA10 (deep red) and EphB6 (olive) pseudokinases, superimposed on that of IRK (black) in the context of the IRK surface (from PDB: 1IRK). Y1162 in IRK and its EphA10 equivalent (Y801) are labeled.

(**B**) Close-up of interactions involving Y801 for EphA10 (left) and Y1162 for IRK (right). Where Y1162 of IRK interacts with D1132 in the HRD motif and R1136 from the end of the catalytic loop, in EphA10 Y801 retains the arginine interaction (with R774), but interacts with a histidine at the very end of the catalytic loop (H775) making up for the lack of an HRD aspartate (replaced by glycine in EphA10).

(**C**) Close-up of residues around the ATP binding sites of EphA10 (left), and EphB6 (right), colored as above. An AMP-PNP molecule is shown – solid when predicted to bind and transparent when not. Residues are shown from the DFG motif (GFG in EphA10, and RLG in EphB6) – and 4 residues beyond – as well as the β5/αD hinge.

See also Figure S3.

FIGURE 4

Comparison of pseudokinase domain dynamics by HDX

(**A**) HDX data at 1 minute for unphosphorylated IRK across 73 peptides (represented as short horizontal lines). Lines are colored according to percent exchange at 1 min (using the scale at right). Secondary structure of IRK is shown at top. Data for longer timepoints are plotted in the lower part of the figure, with the x-axis representing the median residue number of the peptide. Locations of the β5/αD hinge, HRD motif, activation loop (A-loop) and YxxxYY motif are noted. Errors represent SD from three independent labeling experiments.

(**B**) Data (1 min) from the upper part of (**A**) plotted on the (inactive) IRK structure using the same color scheme as in (**A**). Blue represents less, and red more, exchange.

(**C**) Comparison of HDX data (mean ± SD) for PTK7 (slate blue), ROR2 (magenta), RYK (green) and ROR1 (cyan) pseudokinase domains with data for IRK (grey) at 10 s, 1 min, 10 min, and 2 h. X-axis represents IRK-equivalent median residue number. IRK data are depicted as the range for each point. Errors represent SD from three independent labeling experiments.

(**D**) Variance of 'exchangeability index' values – determined as in STAR Methods – for pseudokinases versus IRK (expressed as how many times SD/σ was the IRK value away from the pseudokinase mean), plotted on the inactive IRK structure. A location was assigned no color if within 2σ, but colored black or orange as marked if beyond 2σ (95% confidence).

See also Figure S4 and Table S1.

FIGURE 5

ROR1 signaling in BaF3 cells

(**A**) ROR1 and ROR1ΔICR expression in BaF3 stable clones by anti-HA Western blot (with β-tubulin as loading control).

(**B**) BaF3 (parental), BaF3-ROR1 and BaF3-ROR1ΔICR cells were cultured without IL3 or Wnt5a. Cell number was counted using Trypan-blue exclusion at the indicated time points, and plotted (mean ± SD) for 4 independent experiments. Statistical significance is defined: ***$p \leq 0.001$; **$p \leq 0.01$; *$p \leq 0.05$.

(**C**) BaF3, BaF3-ROR1 and BaF3-ROR1ΔICR cells were serum starved overnight, and then treated with recombinant Wnt5a (50 ng/ml) for the indicated times. Cell lysates were immunoblotted with the indicated antibodies. ROR1 or ROR1ΔICR protein levels were determined using anti-HA blotting. A representative of three independent experiments is shown.

(**D**) Proliferation of BaF3 cells expressing different ROR1 variants as noted (in the absence of IL3 or Wnt5a), assessed using the CellTiter-Glow 2.0 Assay 14 days after seeding, and expressed as a fold increase over that seen for parental BaF3 cells. Data are represented as mean values ± SD, for 3 biological repeats. ***$p \leq 0.001$.

(**E**) Assessment of stable BaF3 clones expressing (HA-tagged) wild-type ROR1, a variant with the activation loop YxxxYY motif mutated to FxxxFF (Y641F/Y645F/Y646F), and a K506A-mutated variant by Western blotting with anti-HA and β-tubulin as loading control.

See also Figure S5.

FIGURE 6

Screening for small molecules that bind pseudokinase domains

(**A**) Summary of DSF-based screen for small molecule binders of Wnt-binding RTK

pseudokinases. Hits identified in the ROR1 screen are denoted with horizontal arrows.

Compounds screened, and screening results, are listed in Table S2.

(**B**) Chemical structures of the two ROR1-binding 'hits' from (**A**).

(**C**) T_M shift as a function of GZD824 concentration binding to purified ROR1 pseudokinase

domain (at 2 μM) using DSF, with curve fit as described in STAR Methods. Mean $\pm$ SD is shown

for three independent experiments.

(**D**) Cellular thermal shift assay (CETSA) showing stabilization of ROR1 in cells upon addition of

ponatinib or GZD824. BaF3-ROR1 cells were treated with 10 μM ponatinib or GZD824, and

subjected to the noted temperatures as described in STAR Methods. Cell lysates were blotted

with anti-HA to assess ROR1 levels, and with anti-β-tubulin as a loading control.

(**E**) CETSA data as in (**D**), derived from signal quantification of 3 independent experiments

(mean ± SD), with curves fit as described in STAR Methods. Band intensities were normalized

to the non-heated and non-treated sample for each experiment (set at a value of 1). Control

(grey) curve represents heated samples without added inhibitor.

See also Figure S6 and Table S2.

FIGURE 7

Binding of ponatinib and GZD824 to the ROR1 pseudokinase domain

(**A**) HDX data for ROR1, comparing exchange differences for 62 peptides with- and without

added GZD824 (50 μM) at a representative 1 min timepoint. Color coding is shown in the scale

at bottom, red representing increased HDX upon inhibitor binding, and blue a reduction. Data for

selected peptides (*i*, *ii*, *iii*, and *iv*) are detailed in (**B**). ROR1 secondary structure is shown at top. Values for all time points for three biological replicates are shown in Fig. S7A.

(**B**) HDX data for selected peptides showing HDX with- and without inhibitor across 3 biological replicates (mean ± SD). Data are shown for ponatinib treatment (solid cyan line) and GZD824 treatment (dotted cyan line), for peptides marked in (**A**): *i* (from helix αC); *ii* (from β5/αD hinge); *iii* (from β1/β2 loop); and *iv* (from the activation loop).

(**C**) Structure of ponatinib-bound ROR1 pseudokinase, shown in cyan (ponatinib is black), with side-chains involved in ponatinib binding detailed in the zoomed view.

(**D**) Overlay of the ponatinib-bound ROR1 pseudokinase domain on the ROR2 pseudokinase domain, using only the C-lobe to guide overlay. In comparing these structures, DynDom3D (Girdlestone and Hayward, 2016) identified an ~20° rotation of the N-lobe with respect to the C-lobe about the yellow near-vertical axis as described in the text. The hinge tyrosine (Y554 in ROR1, Y555 in ROR2) and ROR1 αC helices that interact with ponatinib are labeled, and the displacement of this tyrosine by ponatinib is depicted with a red arrow.

See also Figure S7 and Table S1.

Table 1. Crystallization Conditions, Data Collection and Refinement Statistics

Protein	PTK7	RYK	ROR1-ponatinib
PBD ID	6VG3	6TUA	6TU9
Crystallization Conditions	11 mg/ml protein, 100 mM ADA (pH 6.5), 100 mM $(NH_4)_2SO_4$, 30% (w/v) PEG monoethyl ether 5000, 20˚C	11 mg/ml protein, 100 mM HEPES (pH 7.5), 1.5 M Li_2SO4, 20˚C	13 mg/ml protein, 0.5 mM ponatinib, 100 mM MES (pH 7.2), 12% (w/v) PEG 20K, 4˚C
Data Collection[a]			
Beamline	APS/NE-CAT 24-ID-C	SLS X06SA	SLS X06SA
Date of collection	June 20, 2017	December 7, 2018	December 7, 2018
Wavelength (Å)	0.979	0.99999	0.99999
Space Group	*C 2 2 2₁*	*I 2*	*P 2₁*
Cell Dimensions			
a, b, c (Å)	95.63, 119.92, 166.52	60.64, 47.24, 152.74	54.29, 85.97, 72.98
α, β, γ (°)	90, 90, 90	90.00, 97.64, 90.00	90.00, 91.05, 90.00
Resolution (Å)	48.7 – 1.95	37.85 – 2.38	39.12 – 1.94
Completeness	98.5 (97.7)	98.3 (96.3)	98.7 (97.5)
Redundancy	8.1 (8.1)	3.7 (3.6)	5.0 (5.0)
R_{sym} (%)	9.2 (102.1)	6.4 (38.6)	5.8 (52.1)
I/σ	13.4 (1.9)	8.3 (2.0)	8.0 (2.0)
$CC^{1/2}$ [b]	0.999 (0.74)	1.0 (0.9)	1.0 (0.8)
Refinement			
Number of reflections	68,916 (9835)	17,213 (1691)	49,066 (4844)
R_{work}/R_{free} (%)	18.4/22.9	19.4/24.8	20.9/24.1
Number of atoms			
Protein	6516	2270	4000
Ions	0	25	0
Ligands	0	0	78
Water	598	28	94
Average B factor (Å)			
Protein	45.5	40.3	47.9
Ions	-	92.4	-
Ligands	-	-	37.9
Water	36.2	33.9	42.0
Ramachandran favored (%)	96.4	97.6	96.5
Ramachandran allowed (%)	3.6	2.1	3.5
Ramachandran outliers (%)	0.0	0.4	0.0
Bond length rmsd (Å)	0.009	0.008	0.007
Bond angle rmsd (Å)	1.01	0.88	0.84

[a]Numbers in parentheses denote highest resolution shell

[b]$CC^{1/2}$ reported for the highest resolution shell

STAR METHODS

RESOURCE AVAILABILITY

Lead contact for reagent and resource sharing
Further information and requests for resources and reagents should be directed to and will be fulfilled by the Lead Contact, Mark A. Lemmon (mark.lemmon@yale.edu).

Materials availability
Unique and stable reagents generated in this study are available upon request.

Data and code availability
PDB accession codes for the crystallographic coordinates and structure factors reported in this paper are: PDB: 6VG3 (PTK7 pseudokinase domain http://www.rcsb.org/structure/6VG3); PDB: 6TUA (RYK pseudokinase domain http://www.rcsb.org/structure/6TUA); PDB: 6TU9 (ROR1 pseudokinase domain with bound ponatinib http://www.rcsb.org/structure/6TU9). HDX-MS data and datapoints for all peptides are provided in Table S1 (Excel file). Results from the screen in Fig. 6A are provided in Table S2 (Excel file). Source code for determining 'exchangeability indices' in Fig. 4D is available at https://github.com/sheetzjb/RTKpseudokinases. Original gel data have been deposited to Mendeley Data: https://doi.org/10.17632/65v6bff7bm.1

EXPERIMENTAL MODEL DETAILS

Cell culture
Insect cells
Spodoptera frugiperda Sf9 cells were propagated at 27˚C with constant shaking at 120 rpm in serum-free ESF 921 Insect Cell Culture Medium (Expression Systems) containing 50 U/ml penicillin/streptomycin, and were used for production of all proteins except ROR$^{453-752}$ and RYK$^{292-607}$, for which the TriEx variant of Sf9 cells (EMD Millipore) were used – propagating at 27˚C with constant shaking at 90 rpm in serum-free Insect-XPRESS Medium (Lonza). All Sf9 cells were originally established from immature ovaries of female *S. frugiperda* pupae.
Mammalian cells
Mus musculus BaF3 cells (pro B cell line, DSMZ, ACC 300) were grown in RPMI media (Lonza, Basel, Switzerland) supplemented with 10% fetal bovine serum, 2 mM L-glutamine, 100 U/ml penicillin/streptomycin and 10% WEHI supernatant and incubated at 37˚C and 5% CO_2.

METHOD DETAILS

Plasmid construction for recombinant protein expression
Crystallization constructs: PCR was used to amplify DNA encoding residues 774-1069 of human PTK7, 453-752 of human ROR1 and 292-607 of human RYK. For PTK7 an N-terminal hexahistidine tag plus BamHI and HindIII restriction sites were included, and the fragment was subcloned into pFastBac1 (Invitrogen). For ROR1 and RYK, PCR fragments were inserted into the vector pFB-6HZB (Invitrogen) via ligation-independent cloning.
    Hydrogen/Deuterium Exchange-Mass Spectrometry constructs: DNA fragments encoding residues 457-752 of human ROR1, 318-607 of human RYK (including a sequence encoding an N-terminal TEV cleavage site), and 978-1283 of the human insulin receptor were amplified by PCR – to include sequence encoding an N-terminal hexahistidine tag and regions overlapping with the multiple cloning site of pFastbac1. Insert products and PCR-amplified pFastbac1 vector

were digested with DpnI to remove template DNA, and were subsequently ligated using NEBuilder HiFi DNA Assembly Cloning Kit. A construct encoding residues 452-753 of human ROR2 was generated previously (Artim et al., 2012).

Protein production and purification

Protein production for crystallization: For expression of PTK7$^{774-1069}$, Sf9 cells at 2 x 10^6/ml were infected with recombinant baculovirus, and harvested by centrifugation after 3 days. Cells were lysed by sonication in Buffer A [500 ml of 20 mM Tris-HCl (pH 8.0), 300 mM NaCl, 10% (w/v) glycerol, 10 mM imidazole, 10 mM 2-mercaptoethanol, 1 mM PMSF, protease inhibitor cocktail (Roche)], and the lysate was clarified by centrifugation for 30 min at 16,000 rpm at 4˚C. Clarified lysate was then mixed with Ni-NTA (Ni^{2+}-nitrilotriacetate) beads (Qiagen) – pre-washed 3 times with Buffer A – for 1 h at 4˚C. Beads were then washed with 50 column volumes of Buffer A, and bound PTK7$^{774-1069}$ was eluted with increasing concentrations of imidazole in Buffer B (Buffer A + 400 mM imidazole). Eluted protein was further purified using a Fractogel TMAE (trimethylaminoethyl) anion-exchange column (EMD) equilibrated with Buffer AEX [25 mM Tris-HCl (pH 8.3), 10 mM NaCl, 2 mM DTT (dithiothreitol)] followed by a Fractogel SO3$^-$ cation exchange column (EMD) equilibrated with Buffer CEX [20 mM MES (pH 6.0), 150 mM NaCl, 2 mM DTT]. PTK7$^{774-1069}$ was eluted with a gradient from the starting NaCl concentration in the AEX/CEX column buffers to 1 M NaCl. Protein was then subjected to a final step of size-exclusion chromatography using a Superdex 75 10/300 column (GE Healthcare) equilibrated in 20 mM HEPES (pH 7.0), 150 mM NaCl, and 2 mM DTT.

For expressing ROR1 and RYK pseudokinase domains, exponentially growing TriEx cells (2 x 10^6/ml) were infected 1:64 with virus stock, incubated for 66 h at 27˚C with constant shaking, and harvested by centrifugation. Cells were resuspended in lysis buffer (50 mM HEPES pH 7.4, 500 mM NaCl, 20 mM imidazole, 0.5 mM TCEP, 5% glycerol) and lysed by sonication. Lysate was cleared by centrifugation and loaded onto a Ni NTA column. After washing with lysis buffer, the His6-tagged proteins were eluted in lysis buffer containing 300 mM imidazole. N-terminal tags were cleaved using TEV protease during a dialysis step (to remove imidazole). Contaminating proteins, the cleaved tags and TEV protease were then removed with a second Ni-NTA step. Finally, proteins were concentrated and subjected to size exclusion using an S200 16/600 column (GE Healthcare), from which ROR1 and RYK eluted as expected for monomers. Final yields were 2.5 mg/l insect cell medium (ROR1) and 0.4 mg/l insect cell medium (RYK).

Protein production for HDX-MS: For production of ROR1$^{457–752}$, ROR2$^{452–753}$, or RYK$^{318-607}$, Sf9 cells were lysed by sonication in Buffer A [500 ml of 50 mM Tris-HCl (pH 8.0), 300 mM NaCl, 10 mM 2-mercaptoethanol, 1 mM PMSF, protease inhibitor cocktail (Roche)]. Lysate was clarified by centrifugation for 30 min at 16,000 rpm at 4˚C and loaded onto pre-washed a Ni-NTA (1 ml per liter of culture) for 1 h at 4˚C. Beads were then washed with 50 column volumes of Buffer A, and protein eluted with increasing concentrations of imidazole in Buffer B (Buffer A + 400 mM imidazole). Protein was next loaded onto a Fractogel TMAE (trimethylaminoethyl) anion-exchange column (EMD) equilibrated with Buffer AEX [50 mM Tris-HCl (pH 8.0), 20 mM NaCl, 2 mM DTT (dithiothreitol)], and eluted with a NaCl gradient up to 1 M. Eluted fractions were diluted in Buffer CEX [50 mM MES (pH 6.0), 50 mM NaCl, 2 mM DTT] and loaded onto a Fractogel SO3$^-$ cation exchange column (EMD) equilibrated with Buffer CEX, and eluted with a NaCl gradient in Buffer CEX up to 1 M. Protein was then subjected to size-exclusion chromatography using a Superdex 75 10/300 column (GE Healthcare) equilibrated in 20 mM HEPES (pH 7.0), 150 mM NaCl, and 100 µM TCEP [tris-(2-carboxyethyl)phosphine]. The PTK7 pseudokinase for HDX-MS was purified as described above for crystallization. Production of IRK$^{978–1283}$ followed the same procedure as for the RORs and RYK, except that Buffer A included 5% (w/v) glycerol, and the cation exchange step was omitted.

Crystallization

Crystals of PTK7[774-1069] were obtained using the hanging-drop vapor diffusion method, by mixing equal volumes of protein and reservoir solutions and equilibrating over the reservoir solution at 21˚C. The final protein concentration used was 10.5 mg/ml in 20 mM HEPES (pH 7.0), 150 mM NaCl, and 2 mM DTT. Crystals were obtained with a reservoir solution of 30% (w/v) PEG monomethyl ether 5,000, 100 mM ADA (pH 6.5), and 100 mM $(NH_4)_2SO_4$ (Jena Bioscience JBKinase Screen 3; condition D1).

Crystals of the RYK pseudokinase domain were also obtained using the sitting-drop vapor diffusion method, by transferring 130 nl drops of the RYK protein solutions at 11 mg/ml to a 3-well crystallization plate (Swissci) mixed with 70 nl precipitant solution (consisting of 100 mM HEPES (pH 7.5), 1.5 M Li_2SO4) and incubating at 20˚C. Crystals of the ROR1-ponatinib complex were obtained using the same method and volumes, but using 13 mg/ml ROR1 protein, 0.5 mM ponatinib, and a precipitant solution of 100 mM MES (pH 7.2), 12% (w/v) PEG 20K – and with incubation at 4˚C. Before flash-freezing in liquid nitrogen, PTK7 crystals were cryoprotected in reservoir solution containing 10% (w/v) glycerol, and RYK and ROR1-ponatinib crystals were cryoprotected in reservoir solution containing 25% ethylene glycol.

Structure determination

For PTK7, diffraction data were collected at beamline 23ID-C of GM/CA at Advanced Photon Source (APS) and were processed using HKL2000. PTK7 crystallized in space group $C222_1$ with three molecules in the asymmetric unit. Structures were solved by molecular replacement with Phaser, using co-ordinates for the MuSK TKD (PDB: 1LUF) as a search model (Till et al., 2002). Cycles of manual building/rebuilding using Coot (Emsley and Cowtan, 2004) were alternated with rounds of refinement using REFMAC (CCP4, 1994), plus composite omit maps calculated with CNS. PROCHECK identified no residues in the disallowed region of the Ramachandran plot. For RYK and ROR1/ponatinib, data were collected at Swiss Light Source (SLS) and analyzed, scaled and merged with Xia2 (Winter et al., 2013). Structures were solved by molecular replacement with Phaser using a ROR2 model (PDB: 4GT4) as a template for ROR1 (Artim et al., 2012) and an AXL model (PDB: 5TC0) as a template for RYK (Keung et al., 2017). The resulting models were refined with REFMAC5 (CCP4, 1994) and validated using MolProbity (Chen et al., 2010). Data collection and refinement statistics are listed in Table 1.

Hydrogen-Deuterium Exchange Mass Spectrometry (HDX-MS)

To obtain mass spectra of undeuterated and of D_2O-labelled peptides, purified protein (IRK[978–1283], PTK7[774-1069], ROR1[457-752], ROR2[452–753], or RYK[318-607]) at 0.4 mg/ml in H_2O-based buffer (20 mM HEPES pH 7.4, 200 mM NaCl, 100 µM TCEP) was diluted twenty-fold with either H_2O-containing (undeuterated standards) or D_2O-containing (labeling conditions) buffer (20 mM HEPES pD 7.4, 200 mM NaCl, 100 µM TCEP using deuterium as solvent) to label amide hydrogen atoms (with final 95% D_2O concentration). Labeling was performed at 25˚C for a range of times (10 s, 1 min, 10 min, 1 h, or 2 h), and the reaction was quenched by adding cold (4˚C) 100 mM sodium phosphate buffer at pH 2.4, containing 2 M guanidine hydrochloride and 1% formic acid. For investigating the effect of GZD824 or ponatinib binding on ROR1, ROR1[457-752] (10 µM) was incubated with freshly prepared GZD824 or ponatinib at a final inhibitor concentration of 50 µM (and final DMSO concentration of 5% v/v) for 30 min at 25˚C prior to deuterium labeling. The D_2O buffer contained 20 mM HEPES (pD 7.4), 200 mM NaCl, 50 µM GZD824 or ponatinib (and a final 5% DMSO), and the labeled sample was quenched by adding cold (4˚C) 200 mM sodium phosphate buffer (pH 2.4) containing 2 M guanidine hydrochloride and 1% formic acid. Quenched samples were immediately injected onto a Waters HDX nanoAcquity UPLC (Waters, Milford, MA) with in-line digestion using an Enzymate BEH pepsin column (Waters, Milford, MA). Peptic fragments were trapped on an

Acquity UPLC BEH C18 peptide trap and separated on an Acquity UPLC BEH C18 column. For IRK samples, a CSH C18 peptide trap and column were instead used for a more optimal peptide separation. A 7 min, 5-35% acetonitrile (0.1% Formic acid) gradient was used to elute peptides directly into a Waters Synapt G2-Si mass spectrometer in TOF mode – except for one biological replicate each of ROR1 unliganded, 5% DMSO, and 50 µM GZD824, which were collected using a Waters Xevo G2-XS QTOF mass spectrometer. MS[E] data were acquired with a 15 to 30 V ramp CID for high energy acquisition of product ions as well as continuous lock mass (Leu-Enk) for mass accuracy correction. Peptide identification and protein sequence coverage maps were obtained from the undeuterated controls. Peptides were identified using the ProteinLynx Global SERVER 3.0.3 (PLGS) from Waters. Fully deuterated controls were performed by incubating in the presence of 2 M Guanidine-DCl for two hours prior to quenching (PTK7) or by incubating in D_2O buffer for 2-7 days (ROR1, ROR2, RYK, IRK). All deuterium labeling time points and controls were repeated three times. Data and statistical analyses were carried out as described previously (Houde et al., 2011). Briefly, the deuterium uptake by the identified peptic fragments through increasing deuteration time and for the fully deuterated control was determined using DynamX 3.0 (Waters). The normalized percentage of deuterium uptake at incubation time t ($\%D_t$) at an incubation time t for a given peptide was calculated as follows:

$$\%D_t = 100 * \frac{(m_t - m_0)}{(m_f - m_0)}$$

With m_t being the centroid mass at incubation time t, m_0 the centroid mass of the undeuterated control and m_f the centroid mass of the fully deuterated control. For studies of changes in ROR1 dynamics upon inhibitor binding, the percent deuteration difference plots $\Delta\%D_{exchange}$ (bound-unbound) presented in Fig. 7 were generated by subtracting the corresponding percent deuteration at incubation time t calculated for the DMSO control (unbound) from that calculated with ponatinib or GZD824 (bound) thus:

$$\Delta\%D_{exchange} = \%D_{x,t}(bound) - \%D_{x,t}(unbound)$$

where x is each peptide, and t is the D_2O incubation time. A summary of the HDX-MS data collected and the HDX uptake data are included in Table S1 following consensus guidelines (Masson et al., 2019).

Differential scanning fluorimetry (DSF)
For thermal shift assays to study ATP binding in Fig. S4B, proteins were diluted in 20 mM HEPES (pH 7.5), 150 mM NaCl, and 100 µM TCEP to a final protein concentration of 5 µM. Nucleotide (5 mM) and/or $MgCl_2$ (10 mM) was added. SYPRO Orange (ThermoFisher Scientific) was then added (diluting 2500-fold into the sample), and 25 µl of the reaction mixtures were transferred to Concord 96-well polycarbonate PCR plates (Bio-Rad) with three technical replicates per condition. A Bio-Rad CFX96 Touch Real Time PCR machine was then used to monitor fluorescence at 530 nm while the temperature was raised by 1˚C per minute from 25˚C to 95˚C, with fluorescence measured at each increment. Fluorescence values were then plotted as a function of temperature after normalizing to the maximum fluorescence signal. Melting temperatures (T_M) were determined as the temperature at half-maximum fluorescence. Plots were generated using GraphPad Prism and represent the mean from three technical replicates.

For thermal shift assays used for small molecule screening (Fig. 6) and analysis of ponatinib binding (Fig. 6C), a 2 µM solution of the relevant purified pseudokinase domain in

assay buffer (20 mM HEPES pH 7.4, 150 mM NaCl, 0.5 mM TCEP, 5% glycerol) was mixed 1:1000 with SYPRO Orange (Millipore Sigma). Test compounds were added to a final concentration of 10 μM (containing a final 2% DMSO). 20 μl of each sample were then placed in a 96-well plate, and the temperature increased stepwise from 25°C to 95°C. Fluorescence was monitored using a Mx3005P real-time PCR instrument (Stratagene) with excitation and emission filters set to 465 and 590 nm, respectively. Data were analyzed using MxPro software. Compound screening was performed as a single shot experiment. Potential pseudokinase binders were confirmed by repeating the experiment with an inhibitor concentration series (final concentrations up to 25 µM) – as seen for GZD824 in Fig. 6C. Plots were generated using GraphPad Prism and represent the mean from three technical replicates.

Small molecule screening
Small molecule screening was performed using the DSF assay described above. Our screening collection consisted of the kinase inhibitor library (#L1200 Selleckchem) and FDA-approved drug library (#L1300 Selleckchem), which includes a total of 1486 compounds. Failure to get hits with other pseudokinases does not simply reflect protein stability; the most stable Wnt-signaling pseudokinase was PTK7 (T_M ~ 59°C) followed by RYK (54°C), ROR1 (53°C) and ROR2 (51°C).

Homology models of EphA10 and EphB6
The crystal structure of EphB3 kinase (PDB: 3ZFY) in the inactive conformation (Overman et al., 2014) was selected as the template for modeling the inactive conformation of the EphA10 and EphB6 pseudokinase domains. After running BLAST for sequence alignment, the top crystal structure matches with EphA10 and EphB6 were found to be EphA4 (PDB: 2YGM) and EphB1 (PDB: 3ZFX) respectively, which were then used as templates for modeling active conformations of EphA10 and EphB6 pseudokinase domains. Coordinates of the active and inactive template kinases were downloaded from the Protein Data Bank, and missing residues were added by generating a homology model of the kinase using its own partial structure as the template. Five candidate models were generated from each of the templates by satisfying a set of static and dynamic spatial restraints in MODELLER. These restraints are expressed in terms of molecular probability density function, or objective function, which is optimized and applied in the ranking of the set of models constructed in MODELLER. The stereochemical quality of each model was further evaluated using the Discrete Optimized Protein Energy (DOPE) method – an atomic distance-dependent statistical potential optimized for model assessment in MODELLER, with the lowest DOPE score defining the preferred model. We structurally aligned all of the homology models for EphA10 and EphB6 to their template structures using Visual Molecular Dynamics (VMD), and generated Root Mean Square Deviation (RMSD) plots to find regions of variability. Most variation was seen in the first 50 residues for the homology models of the inactive structures of EphA10 and EphB6, so a hybrid approach was used to improve models for the inactive EphA10 and EphB6 conformations, where the coordinates for the first 50 residues came from the homology model for the active conformation of the kinase, and the rest of the coordinates come from the homology model for the inactive conformation. VMD was used to display structural models, and MODELLER was used for homology modeling of the pseudokinase domains for both EphA10 and EphB6.

BaF3 cell transfections
For expression in BaF3 cells, human ROR1, ROR2, PTK7 and RYK (or their truncated variants) were cloned into the pEFIRES-P vector (Hobbs et al., 1998) and electroporated into BaF3 cells using the 4D-Nucleofector X Kit L (Lonza) and a 4D Nucleofector X (Lonza), using program

code DS-137. After 72 h, transfected cells were selected with increasing amounts of puromycin (0.5-1 μg/ml) for 2 weeks and tested for protein expression by Western blot (Figs. 5 and S5).

Cell viability and cell proliferation
Cell counts were determined by Trypan-blue exclusion using a Countess II automated cell counter (Life Technologies). Cell viability was measured using the CellTiter-Glow 2.0 Assay (CTG, Promega, Madison, USA) according to the manufacturer's instructions.

Western blotting
Whole cell lysates were prepared by lysing cells in ice cold NP-40 lysis buffer (50 mM Tris-HCl pH 7.4, 10% glycerol, 50 mM NaCl, 0.5% sodium deoxycholate, 1% NP-40, 20 mM NaF), supplemented with protease and phosphatase inhibitor cocktails (Bimake, Houston, TX, USA). Cell lysates were incubated 15 min on ice, clarified by centrifugation (4°C, 20 min, 20,000 x g), resuspended in 2 x SDS sample buffer and boiled at 95°C for 5 min. Samples were separated by SDS-PAGE and transferred to nitrocellulose membrane. Blots were blocked (4% BSA in 0.05% Tween 20 in 1xTBS) at RT for 1 h and incubated with primary antibody at 4°C overnight. Blots were then washed 3 times with TBS/0.1% Tween 20 buffer, and subjected to secondary antibodies for 1 h at RT. Blots were scanned with an Odyssey® CLx Imaging System (LI-COR) and images analyzed using Image Studio Lite (LI-COR).

   For Western blotting, the following antibodies were used: pAKT (S473, #6942), AKT (#9272), pERK1/2 (#9101), ERK1/2 (#4696), PTK7 (#25618), and SRC (#2109) from Cell Signaling Technology (Danvers, MA, USA); ROR1 4A5 (#564464) and ROR2 (#565550) from BD Biosciences (San Jose, CA, USA); anti-pTYR 4G10 (#05-321) from MerckMillipore; β-tubulin (#sc-166729) from Santa Cruz Biotechnology (Dallas, TX, USA); HA (#901513) from BioLegend (San Diego, CA). As secondary antibodies, IRDye® 800CW Donkey anti-Mouse IgG or IRDye® 680RD Donkey anti-Rabbit IgG (LI-COR, Lincoln, NE, USA) were used at 1:10.000 dilution.

Cellular thermal shift assay (CETSA)
CETSA was carried out according to the protocol described (Martinez Molina et al., 2013). Briefly, BaF3-ROR1 cells were treated with control (DMSO) or drug (10 μM) and incubated at 37°C for 2 h. Cells were washed once and divided into aliquots with 0.5 x 10^6 cells each. Samples were heated (Bio-Rad T100TM Thermal Cycler) pairwise (control and drug-treated samples) for 3 min at 42-60°C with 2°C increments between pairs. After heating, cells were kept at room temperature for 3 min before transferring to ice. Cells were collected and lysed in Triton X100-containing lysis buffer (50 mM Tris-HCl, pH 7.5, 10% glycerol, 150 mM NaCl, 1 mM EDTA, 1% Triton X-100, 50 mM NaF) supplemented with protease and phosphatase inhibitor cocktails (Bimake, Houston, TX, USA), and were subsequently analyzed by SDS-PAGE and Western blotting using anti-HA (ROR1) and β-tubulin antibodies. Protein levels were quantified with Image Studio Lite (Li-COR) and normalized to 42°C samples for both treatments.

in vitro kinase assays
Kinase assays were performed using either ATP hydrolysis as a readout (ADP-Glo) or fluorescence detection of phosphorylation of a peptide. For the ADP-Glo assay (Promega), a kit was used as recommended by the manufacturer. Briefly, reactions with 1 μM purified ROR1 pseudokinase domain or kinase controls (at 1 μM) were set up in kinase assay buffer (20 mM HEPES, pH 7.4, containing 10 mM MgCl$_2$, 0.02 mg/ml BSA, 0.1 mM Na$_3$VO$_4$, 2 mM DTT) with addition of 1 mM ATP and 0.1 mg/ml poly(Glu, Tyr) peptide substrate (Sigma-Aldrich). Reactions were incubated for 1 h at ambient temperature, and were then quenched by addition of an equal volume of ADP-Glo reagent – unreacted ATP was depleted over the course of 40 minutes at room temperature. An equal volume of detection reagent was then added to convert

ADP in the reaction mixture into newly synthesized ATP, which serves as a substrate for the luciferase reaction. Samples were incubated for 1 h at room temperature before luminescence measurements were taken in a 384-well plate using a BioTek Synergy 2 Multi-Detection Microplate Reader. Experiments were performed in technical triplicate.

For fluorescent peptide assays, materials from Assay Quant Technologies were used as recommended by the manufacturer. Briefly, reactions with 1 μM purified ROR1 pseudokinase domain or kinase controls (at 1 μM) were set up in wells of a 384-well plate with the final assay conditions: 50 mM HEPES, pH 7.5, containing 10 mM $MgCl_2$, 0.01% Brij-35, 0.1 mg/ml BSA, 1 mM ATP, and 20 μM peptide substrate sensor (AQT0001) that contains an incorporated Sox chromophore (Assay Quant). Reactions were incubated at 30°C for 2 h, and fluorescence intensities were collected every 2 min using a BioTek Synergy 2 Multi-Detection Microplate Reader. Experiments were performed in technical triplicate.

QUANTIFICATION AND STATISTICAL ANALYSIS

Structure determination and analysis
The statistical analysis of the structural models is provided in Table 1. Analysis of the molecular contacts and RMSD values were calculated using the CCP4 software package (CCP4, 1994).

Analysis of HDX dynamics
Raw MS^E mass spectra of undeuterated controls were used for peptide identification using ProteinLynx Global Server 3.0.3 (PLGS) from Waters. MS data from all controls and labeling conditions were then processed using DynamX to identify peptic peptides for each condition. All raw spectra for each peptide, labeling condition, drug condition, and charge state were then manually assessed for quality and for accurate peak assignment, at which point poor quality or incorrectly assigned peaks were unassigned. Average mass shifts of centroids and their standard deviations were then used to calculate percent uptake for each time point relative to a fully deuterated standard as described in Method Details. Uptake plots in Figs. 4A,C represent standard deviations from three independent labeling experiments for all conditions shown. Uptake plots in Fig. 7B represent mean ± SD from three independent protein preparations, for each of which three independent labelling experiments were performed in all conditions.

For 'exchangeability indices' (Fig. 4D), an R script was written to first calculate an average percent exchange for each residue in each pseudokinase (and IRK) at each time point. The value assigned to each residue was the mean (per residue) percent exchange seen for all peptides containing that residue. In parallel, each residue in each pseudokinase was assigned a corresponding homologous residue in IRK (based on sequence alignments). For the position corresponding to each residue in IRK, the mean ($\pm$ SD) percent exchange was calculated across the 4 pseudokinases (ROR1, ROR2, RYK, PTK7) for each time point. This pseudokinase 'exchangeability index' value was then compared with the exchange value assigned to the corresponding residue in IRK – with deviations reported in terms of number of standard deviations (σ) away from the average pseudokinase uptake. Differences between pseudokinase exchangeability index and IRK exchange for each residue were averaged across all time points to depict areas that show more (orange) or less (black) HDX in pseudokinases than in IRK, as shown in Fig. 4D.

Western blot image processing
Raw images from the LI-COR Odyssey were imported in Adobe Photoshop, and linear contrast stretching was manually applied using the 'Levels' function – so that the darkest

points of the images are black, and background is brought into the visible grey scale so that all features are registered.

Cell proliferation assays
All cell proliferation assays experiments were analyzed using Prism v8.0 software (GraphPad, San Diego, CA, USA). Cell proliferation data are represented as mean ± SD from four independent experiments each performed in technical triplicate. Statistical significance was determined using two-tailed t-tests. Two-sided p values were used to determine statistical significance, set as follows: *$p \leq 0.05$, **$p \leq 0.01$ and ***$p \leq 0.001$.

Cellular thermal shift assays
All cellular thermal shift experiments were analyzed using Prism v8.0 software (GraphPad, San Diego, CA, USA). Individual bands were quantified using Image Studio Lite software and all values (band intensities) were normalized to unheated control sample (no inhibitor treatment) that denotes relative band intensity value of one. Standard deviation (SD) was calculated using three independent experiments. Curve fitting was done in Prism using Boltzmann sigmoidal algorithm. For concentration-dependent CETSA in Fig. S6, a constant heating temperature of 48˚C was chosen based on the results from Fig. 6E. All values (band intensities) were normalized to heated samples without inhibitor. Curve fitting was done in Prism using one site (specific binding) algorithm.

SUPPLEMENTAL EXCEL TABLE TITLES

TABLE S1 – Related to Figures 4 and 7.
HDX-MS summary and uptake data.
Experimental details are listed for all HDX-MS experiments performed in this study, and the uptake data for each peptide reported are included.

TABLE S2 – Related to Figure 6.
Compound list and results for screening to identify pseudokinase-binding molecules.
A library of 1486 small molecules consisting largely of protein kinase inhibitors or FDA approved drugs and their respective effects on the differential scanning fluorometry-based T_m shift values of PTK7, ROR1, ROR2, and RYK.

REFERENCES

Ablooglu, A.J., Frankel, M., Rusinova, E., Ross, J.B., and Kohanski, R.A. (2001). Multiple activation loop conformations and their regulatory properties in the insulin receptor's kinase domain. J. Biol. Chem. *276*, 46933-46940.

Adams, P.D., Afonine, P.V., Bunkoczi, G., Chen, V.B., Davis, I.W., Echols, N., Headd, J.J., Hung, L.W., Kapral, G.J., Grosse-Kunstleve, R.W., et al. (2010). PHENIX: a comprehensive Python-based system for macromolecular structure solution. Acta Crystallogr. D Biol. Crystallogr. *66*, 213-221.

Akbarzadeh, S., Wheldon, L.M., Sweet, S.M., Talma, S., Mardakheh, F.K., and Heath, J.K. (2008). The deleted in brachydactyly B domain of ROR2 is required for receptor activation by recruitment of Src. PLoS One *3*, e1873.

Amin, D.N., Campbell, M.R., and Moasser, M.M. (2010). The role of HER3, the unpretentious member of the HER family, in cancer biology and cancer therapeutics. Semin. Cell Dev. Biol. *21*, 944-950.

Artim, S.C., Mendrola, J.M., and Lemmon, M.A. (2012). Assessing the range of kinase autoinhibition mechanisms in the insulin receptor family. Biochem. J. *448*, 213-220.

Bailey, F.P., Byrne, D.P., McSkimming, D., Kannan, N., and Eyers, P.A. (2015). Going for broke: targeting the human cancer pseudokinome. Biochem. J. *465*, 195-211.

Becher, I., Savitski, M.M., Savitski, M.F., Hopf, C., Bantscheff, M., and Drewes, G. (2013). Affinity profiling of the cellular kinome for the nucleotide cofactors ATP, ADP, and GTP. ACS Chem. Biol. *8*, 599-607.

Bicocca, V.T., Chang, B.H., Masouleh, B.K., Muschen, M., Loriaux, M.M., Druker, B.J., and Tyner, J.W. (2012). Crosstalk between ROR1 and the Pre-B cell receptor promotes survival of t(1;19) acute lymphoblastic leukemia. Cancer Cell *22*, 656-667.

Boudeau, J., Miranda-Saavedra, D., Barton, G.J., and Alessi, D.R. (2006). Emerging roles of pseudokinases. Trends Cell Biol. *16*, 443-452.

Bunney, T.D., Inglis, A.J., Sanfelice, D., Farrell, B., Kerr, C.J., Thompson, G.S., Masson, G.R., Thiyagarajan, N., Svergun, D.I., Williams, R.L., et al. (2018). Disease variants of FGFR3 reveal molecular basis for the recognition and additional roles for Cdc37 in Hsp90 chaperone system. Structure *26*, 446-458.

Burslem, G.M., Smith, B.E., Lai, A.C., Jaime-Figueroa, S., McQuaid, D.C., Bondeson, D.P., Toure, M., Dong, H., Qian, Y., Wang, J., et al. (2018). The advantages of targeted protein degradation over inhibition: An RTK case study. Cell Chem. Biol. *25*, 67-77.

CCP4 (1994). The CCP4 suite: Programs for protein crystallography. Acta Crystallogr. D Biol. Crystallogr. *50*, 760–763.

Chen, V.B., Arendall, W.B., 3rd, Headd, J.J., Keedy, D.A., Immormino, R.M., Kapral, G.J., Murray, L.W., Richardson, J.S., and Richardson, D.C. (2010). MolProbity: all-atom structure validation for macromolecular crystallography. Acta Crystallogr. D Biol. Crystallogr. *66*, 12-21.

Choi, M.Y., Widhopf, G.F., 2nd,, Ghia, E.M., Kidwell, R.L., Hasan, M.K., Yu, J., Rassenti, L.Z., Chen, L., Chen, Y., Pittman, E., et al. (2018). Phase I trial: Cirmtuzumab inhibits ROR1 signaling and stemness signatures in patients with chronic lymphocytic leukemia. Cell Stem Cell *22*, 951-959.

Choi, M.Y., Widhopf, G.F., 2nd,, Wu, C.C., Cui, B., Lao, F., Sadarangani, A., Cavagnaro, J., Prussak, C., Carson, D.A., Jamieson, C., et al. (2015). Pre-clinical specificity and safety of UC-

961, a first-in-class monoclonal antibody targeting ROR1. Clin. Lymph. Myeloma Leuk. *15*, S167-S169.

Collins, M.K., Downward, J., Miyajima, A., Maruyama, K., Arai, K., and Mulligan, R.C. (1988). Transfer of functional EGF receptors to an IL3-dependent cell line. J. Cell. Physiol. *137*, 293-298.

Damelin, M., Bankovich, A., Bernstein, J., Lucas, J., Chen, L., Williams, S., Park, A., Aguilar, J., Ernstoff, E., Charati, M., et al. (2017). A PTK7-targeted antibody-drug conjugate reduces tumor-initiating cells and induces sustained tumor regressions c. Sci. Transl. Med. *9*, eaag2611.

Daneshmanesh, A.H., Porwit, A., Hojjat-Farsangi, M., Jeddi-Tehrani, M., Tamm, K.P., Grandér, D., Lehmann, S., Norin, S., Shokri, F., Rabbani, H., et al. (2013). Orphan receptor tyrosine kinases ROR1 and ROR2 in hematological malignancies. Leuk. Lymphoma *54*, 843-850.

Debebe, Z., and Rathmell, W.K. (2015). Ror2 as a therapeutic target in cancer. Pharmacol. Ther. *150*, 143-148.

Dhawan, N.S., Scopton, A.P., and Dar, A.C. (2016). Small molecule stabilization of the KSR inactive state antagonizes oncogenic Ras signalling. Nature *537*, 112-116.

Dong, J., Zhao, H., Zhou, T., Spiliotopoulos, D., Rajendran, C., Li, X.D., Huang, D., and Caflisch, A. (2014). Structural analysis of the binding of type I, I1/2, and II inhibitors to Eph tyrosine kinases. ACS Med. Chem. Lett. *6*, 79-83.

Emsley, P., and Cowtan, K. (2004). Coot: model-building tools for molecular graphics. Acta Crystallogr. D Biol. Crystallogr. *60*, 2126-2132.

Fedorov, O., Niesen, F.H., and Knapp, S. (2012). Kinase inhibitor selectivity profiling using differential scanning fluorimetry. Methods Mol. Biol. *795*, 109-118.

Gentile, A., Lazzari, L., Benvenuti, S., Trusolino, L., and Comoglio, P.M. (2011). Ror1 is a pseudokinase that is crucial for Met-driven tumorigenesis. Cancer Res. *71*, 3132-3141.

Gentile, A., Lazzari, L., Benvenuti, S., Trusolino, L., and Comoglio, P.M. (2014). The ROR1 pseudokinase diversifies signaling outputs in MET-addicted cancer cells. Int. J. Cancer *135*, 2305-2316.

Girdlestone, C., and Hayward, S. (2016). The DynDom3D Webserver for the analysis of domain movements in multimeric proteins. J. Comput. Biol. *23*, 21-26.

Green, J., Nusse, R., and van Amerongen, R. (2014). The role of Ryk and Ror receptor tyrosine kinases in Wnt signal transduction. Cold Spring Harb. Perspect. Biol. *6*, a009175.

Gustafson, W.C., Meyerowitz, J.G., Nekritz, E.A., Chen, J., Benes, C., Charron, E., Simonds, E.F., Seeger, R., Matthay, K.K., Hertz, N.T., et al. (2014). Drugging MYCN through an allosteric transition in Aurora kinase A. Cancer Cell *26*, 414-427.

Hammaren, H.M., Ungureanu, D., Grisouard, J., Skoda, R.C., Hubbard, S.R., and Silvennoinen, O. (2015). ATP binding to the pseudokinase domain of JAK2 is critical for pathogenic activation. Proc. Natl. Acad. Sci. U. S. A. *112*, 4642-4647.

Hayes, M., Naito, M., Daulat, A., Angers, S., and Ciruna, B. (2013). Ptk7 promotes non-canonical Wnt/PCP-mediated morphogenesis and inhibits Wnt/β-catenin-dependent cell fate decisions during vertebrate development. Development *140*, 1807-1818.

Hobbs, S., Jitrapakdee, S., and Wallace, J.C. (1998). Development of a bicistronic vector driven by the human polypeptide chain elongation factor 1alpha promoter for creation of stable mammalian cell lines that express very high levels of recombinant proteins. Biochem. Biophys. Res. Commun. *252*, 368-372.

Hornbeck, P.V., Zhang, B., Murray, B., Kornhauser, J.M., Latham, V., and Skrzypek, E. (2015). PhosphoSitePlus, 2014: mutations, PTMs and recalibrations. Nucleic Acids Res. *43(Database issue)*, D512-D520.

Houde, D., Berkowitz, S.A., and Engen, J.R. (2011). The utility of hydrogen/deuterium exchange mass spectrometry in biopharmaceutical comparability studies. J. Pharm. Sci. *100*, 2071-2086.

Hsu, Y.H., Johnson, D.A., and Traugh, J.A. (2008). Analysis of conformational changes during activation of protein kinase Pak2 by amide hydrogen/deuterium exchange. J. Biol. Chem. *283*, 36397-36405.

Hubbard, S.R. (2013). The insulin receptor: both a prototypical and atypical receptor tyrosine kinase. Cold Spring Harb. Perspect. Biol. *5*, a008946.

Hubbard, S.R., Wei, L., Ellis, L., and Hendrickson, W.A. (1994). Crystal structure of the tyrosine kinase domain of the human insulin receptor. Nature *372*, 746-754.

Hunter, J.D. (2007). Matplotlib: A 2D graphics environment. Computing in Science and Engineering *9*, 90-95.

Huse, M., and Kuriyan, J. (2002). The conformational plasticity of protein kinases. Cell *109*, 275-282.

Iacob, R.E., Pene-Dumitrescu, T., Zhang, J., Gray, N.S., Smithgall, T.E., and Engen, J.R. (2009). Conformational disturbance in Abl kinase upon mutation and deregulation. Proc. Natl. Acad. Sci. U. S. A. *106*, 1386-1391.

Inoue, T., Oz, H.S., Wiland, D., Gharib, S., Deshpande, R., Hill, R.J., Katz, W.S., and Sternberg, P.W. (2004). *C. elegans* LIN-18 is a Ryk ortholog and functions in parallel to LIN-17/Frizzled in Wnt signaling. Cell *118*, 795-806.

Jacob, W., James, I., Hasmann, M., and Weisser, M. (2018). Clinical development of HER3-targeting monoclonal antibodies: Perils and progress. Cancer Treat. Rev. *68*, 111-123.

Jacobsen, A.V., and Murphy, J.M. (2017). The secret life of kinases: insights into non-catalytic signalling functions from pseudokinases. Biochem. Soc. Trans. *45*, 665-681.

Jaiswal, B.S., Kljavin, N.M., Stawiski, E.W., Chan, E., Parikh, C., Durinck, S., Chaudhuri, S., Pujara, K., Guillory, J., Edgar, K.A., et al. (2013). Oncogenic ERBB3 mutations in human cancers. Cancer Cell *23*, 603-617.

Jura, N., Shan, Y., Cao, X., Shaw, D.E., and Kuriyan, J. (2009). Structural analysis of the catalytically inactive kinase domain of the human EGF receptor 3. Proc. Natl. Acad. Sci. U. S. A. *106*, 21608-21613.

Jura, N., Zhang, X., Endres, N.F., Seeliger, M.A., Schindler, T., and Kuriyan, J. (2011). Catalytic control in the EGF receptor and its connection to general kinase regulatory mechanisms. Mol. Cell *42*, 9-22.

Karvonen, H., Barker, H., Kaleva, L., Niininen, W., and Ungureanu, D. (2019). Molecular mechanisms associated with ROR1-mediated drug resistance: Crosstalk with Hippo-YAP/TAZ and BMI-1 pathways. Cells *8*, E812.

Karvonen, H., Perttilä, R., Niininen, W., Barker, H., and Ungureanu, D. (2018). Targeting Wnt signaling pseudokinases in hematological cancers. Eur. J. Haematol. *101*, 457-465.

Katoh, M. (2017). Canonical and non-canonical WNT signaling in cancer stem cells and their niches: Cellular heterogeneity, omics reprogramming, targeted therapy and tumor plasticity Int. J. Oncol. *51*, 1357-1369.

Katso, R.M., Russell, R.B., and Ganesan, T.S. (1999). Functional analysis of H-Ryk, an atypical member of the receptor tyrosine kinase family. Mol. Cell. Biol. *19*, 6427-6240.

Keung, W., Boloor, A., Brown, J., Kiryanov, A., Gangloff, A., Lawson, J.D., Skene, R., Hoffman, I., Atienza, J., Kahana, J., et al. (2017). Structure-based optimization of 1H-imidazole-2-carboxamides as Axl kinase inhibitors utilizing a Mer mutant surrogate. Bioorg. Med. Chem. Lett. *27*, 1099-1104.

Kornev, A.P., and Taylor, S.S. (2009). Pseudokinases: functional insights gleaned from structure. Structure *17*, 5-7.

Kornev, A.P., and Taylor, S.S. (2010). Defining the conserved internal architecture of a protein kinase. Biochim. Biophys. Acta *1804*, 440-444.

Kornev, A.P., and Taylor, S.S. (2015). Dynamics-driven allostery in protein kinases. Trends Biochem. Sci. *40*, 628-647.

Kung, A., Chen, Y.C., Schimpl, M., Ni, F., Zhu, J., Turner, M., Molina, H., Overman, R., and Zhang, C. (2016). Development of specific, irreversible inhibitors for a receptor tyrosine kinase EphB3. J. Am. Chem. Soc. *138*, 10554-10560.

Kung, J.E., and Jura, N. (2019). Prospects for pharmacological targeting of pseudokinases. Nat. Rev. Drug Discov. *18*, 501-526.

Lemmon, M.A., and Schlessinger, J. (2010). Cell signaling by receptor tyrosine kinases. Cell *141*, 1117-1134.

Liang, L.Y., Patel, O., Janes, P.W., Murphy, J.M., and Lucet, I.S. (2019). Eph receptor signalling: from catalytic to non-catalytic functions. Oncogene *38*, 6567-6584.

Littlefield, P., Liu, L., Mysore, V., Shan, Y., Shaw, D.E., and Jura, N. (2014). Structural analysis of the EGFR/HER3 heterodimer reveals the molecular basis for activating HER3 mutations. Sci. Signal. *7*, ra114.

Liu, X., Pu, W., He, H., Fan, X., Zheng, Y., Zhou, J.K., Ma, R., He, J., Zheng, Y., Wu, K., et al. (2019). Novel ROR1 inhibitor ARI-1 suppresses the development of non-small cell lung cancer. Cancer Lett. *458*, 76-85.

Loving, H.S., and Underbakke, E.S. (2019). Conformational dynamics of FERM-mediated autoinhibition in Pyk2 tyrosine kinase. Biochemistry *58*, 3767-3776.

Manning, G., Whyte, D.B., Martinez, R., Hunter, T., and Sudarsanam, S. (2002). The protein kinase complement of the human genome. Science *298*, 1912-1934.

Martinez Molina, D., Jafari, R., Ignatushchenko, M., Seki, T., Larsson, E.A., Dan, C., Sreekumar, L., Cao, Y., and Nordlund, P. (2013). Monitoring drug target engagement in cells and tissues using the cellular thermal shift assay. Science *341*, 84-87.

Masson, G.R., Burke, J.E., Ahn, N.G., Anand, G.S., Borchers, C., Brier, S., Bou-Assaf, G.M., Engen, J.R., Englander, S.W., Faber, J., et al. (2019). Recommendations for performing, interpreting and reporting hydrogen deuterium exchange mass spectrometry (HDX-MS) experiments. Nature Methods *16*, 595-602.

McKinney, W. (2010). Data structures for statistical computing in Python. Proceedings of the 9th Python in Science Conference, 51 - 56.

Mendrola, J.M., Shi, F., Park, J.H., and Lemmon, M.A. (2013). Receptor tyrosine kinases with intracellular pseudokinase domains. Biochem. Soc.Trans. *41*, 1029-1036.

Modi, V., and Dunbrack, R.L., Jr. (2019). Defining a new nomenclature for the structures of active and inactive kinases. Proc. Natl. Acad. Sci. U. S. A. *116*, 6818-6827.

Moslin, R., Zhang, Y., Wrobleski, S.T., Lin, S., Mertzman, M., Spergel, S., Tokarski, J.S., Strnad, J., Gillooly, K., McIntyre, K.W., et al. (2019). Identification of N-methyl nicotinamide and N-methyl pyridazine-3-carboxamide pseudokinase domain ligands as highly selective allosteric inhibitors of tyrosine kinase 2 (TYK2. J. Med. Chem. *62*, 8953-8972.

Murphy, J.M., Zhang, Q., Young, S.N., Reese, M.L., Bailey, F.P., Eyers, P.A., Ungureanu, D., Hammaren, H., Silvennoinen, O., Varghese, L.N., et al. (2014). A robust methodology to subclassify pseudokinases based on their nucleotide-binding properties. Biochem. J. *457*, 323-334.

Nagano, K., Maeda, Y., Kanasaki, S., Watanabe, T., Yamashita, T., Inoue, M., Higashisaka, K., Yoshioka, Y., Abe, Y., Mukai, Y., et al. (2014). Ephrin receptor A10 is a promising drug target potentially useful for breast cancers including triple negative breast cancers. J. Control. Release *189*, 72-79.

Novotny, C.J., Pollari, S., Park, J.H., Lemmon, M.A., Shen, W., and Shokat, K.M. (2016). Overcoming resistance to HER2 inhibitors through state-specific kinase binding. Nat. Chem. Biol. *12*, 923-930.

O'Hare, T., Shakespeare, W.C., Zhu, X., Eide, C.A., Rivera, V.M., Wang, F., Adrian, L.T., Zhou, T., Huang, W.S., Xu, Q., et al. (2009). AP24534, a pan-BCR-ABL inhibitor for chronic myeloid leukemia, potently inhibits the T315I mutant and overcomes mutation-based resistance. Cancer Cell *16*, 401-412.

Overman, R.C., Debreczeni, J.E., Truman, C.M., McAlister, M.S., and Attwood, T.K. (2014). Completing the structural family portrait of the human EphB tyrosine kinase domains. Protein Sci. *23*, 627-638.

Patel, O., Griffin, M.D.W., Panjikar, S., Dai, W., Ma, X., Chan, H., Zheng, C., Kropp, A., Murphy, J.M., Daly, R.J., et al. (2017). Structure of SgK223 pseudokinase reveals novel mechanisms of homotypic and heterotypic association. Nat. Commun. *8*, 1157.

Peradziryi, H., Tolwinski, N.S., and Borchers, A. (2012). The many roles of PTK7: a versatile regulator of cell-cell communication. Arch. Biochem. Biophys. *524*, 71-76.

Petrie, E.J., Czabotar, P.E., and Murphy, J.M. (2019). The structural basis of necroptotic cell death signaling. Trends Biochem. Sci. *44*, 53-63.

Prebet, T., Lhoumeau, A.C., Arnoulet, C., Aulas, A., Marchetto, S., Audebert, S., Puppo, F., Chabannon, C., Sainty, D., Santoni, M.J., et al. (2010). The cell polarity PTK7 receptor acts as a modulator of the chemotherapeutic response in acute myeloid leukemia and impairs clinical outcome. Blood *116*, 2315-2323.

Reiterer, V., Eyers, P.A., and Farhan, H. (2014). Day of the dead: pseudokinases and pseudophosphatases in physiology and disease. Trends Cell Biol. *24*, 489-505.

Ren, X., Pan, X., Zhang, Z., Wang, D., Lu, X., Li, Y., Wen, D., Long, H., Luo, J., Feng, Y., et al. (2013). Identification of GZD824 as an orally bioavailable inhibitor that targets phosphorylated and nonphosphorylated breakpoint cluster region-Abelson (Bcr-Abl) kinase and overcomes clinically acquired mutation-induced resistance against imatinib. J. Med. Chem. *56*, 879-894.

Scheeff, E.D., Eswaran, J., Bunkoczi, G., Knapp, S., and Manning, G. (2009). Structure of the pseudokinase VRK3 reveals a degraded catalytic site, a highly conserved kinase fold, and a putative regulatory binding site. Structure *17*, 128-138.

Shan, Y., Gnanasambandan, K., Ungureanu, D., Kim, E.T., Hammarén, H., Yamashita, K., Silvennoinen, O., Shaw, D.E., and Hubbard, S.R. (2014). Molecular basis for pseudokinase-dependent autoinhibition of JAK2 tyrosine kinase. Nat. Struct. Mol. Biol. *21*, 579-584.

Shi, F. (2012). Ph.D. Thesis: Signaling by non-canonical receptor tyrosine kinases ERBB3 and RYK, (University of Pennsylvania). https://repository.upenn.edu/edissertations/699

Shi, F., Telesco, S.E., Liu, Y., Radhakrishnan, R., and Lemmon, M.A. (2010). ErbB3/HER3 intracellular domain is competent to bind ATP and catalyze autophosphorylation. Proc. Natl. Acad. Sci. U. S. A. *107*, 7692-7697.

Shi, Z., Resing, K.A., and Ahn, N.G. (2006). Networks for the allosteric control of protein kinases. Curr. Opin. Struct. Biol. *16*, 686-692.

Sours, K.M., Kwok, S.C., Rachidi, T., Lee, T., Ring, A., Hoofnagle, A.N., Resing, K.A., and Ahn, N.G. (2008). Hydrogen-exchange mass spectrometry reveals activation-induced changes in the conformational mobility of p38alpha MAP kinase. J. Mol. Biol. *379*, 1075-1093.

Steinkamp, M.P., Low-Nam, S.T., Yang, S., Lidke, K.A., Lidke, D.S., and Wilson, B.S. (2014). erbB3 is an active tyrosine kinase capable of homo- and heterointeractions. Mol. Cell. Biol. *34*, 965-977.

Stricker, S., Rauschenberger, V., and Schambony, A. (2017). ROR-family receptor tyrosine kinases. Curr. Top. Dev. Biol. *123*, 105-142.

Till, J.H., Ablooglu, A.J., Frankel, M., Bishop, S.M., Kohanski, R.A., and Hubbard, S.R. (2001). Crystallographic and solution studies of an activation loop mutant of the insulin receptor tyrosine kinase: insights into kinase mechanism. J. Biol. Chem. *276*, 10049-10055.

Till, J.H., Becerra, M., Watty, A., Lu, Y., Ma, Y., Neubert, T.A., Burden, S.J., and Hubbard, S.R. (2002). Crystal structure of the MuSK tyrosine kinase: insights into receptor autoregulation. Structure *10*, 1187-1196.

Tsutsui, Y., Deredge, D., Wintrode, P.L., and Hays, F.A. (2016). Imatinib binding to human c-Src is coupled to inter-domain allostery and suggests a novel kinase inhibition strategy. Sci. Rep. *6*, 30832.

Warmuth, M., Kim, S., Gu, X.J., Xia, G., and Adrián, F. (2007). Ba/F3 cells and their use in kinase drug discovery. Curr. Opin. Oncol. *19*, 55-60.

Waskom, M., Olga, B., O'Kane, D., Hobson, P., Ostblom, J., Lukauskas, S., Gemperline, D.C., Augspurger, T., Halchenko, Y., Cole, J.B., et al. (2018). https://doi.org/10.5281/zenodo.1313201.

Winter, G., Lobley, C.M., and Prince, S.M. (2013). Decision making in xia2. Acta Crystallogr. D. Biol. Crystallogr. *69(Pt 7)*, 1260-1273.

Wrobleski, S.T., Moslin, R., Lin, S., Zhang, Y., Spergel, S., Kempson, J., Tokarski, J.S., Strnad, J., Zupa-Fernandez, A., Cheng, L., et al. (2019). Highly selective inhibition of tyrosine kinase 2 (TYK2) for the treatment of autoimmune diseases: Discovery of the allosteric inhibitor BMS-986165. J. Med. Chem. *62*, 8973-8995.

Wybenga-Groot, L.E., Baskin, B., Ong, S.H., Tong, J., Pawson, T., and Sicheri, F. (2001). Structural basis for autoinhibition of the Ephb2 receptor tyrosine kinase by the unphosphorylated juxtamembrane region. Cell *106*, 745-757.
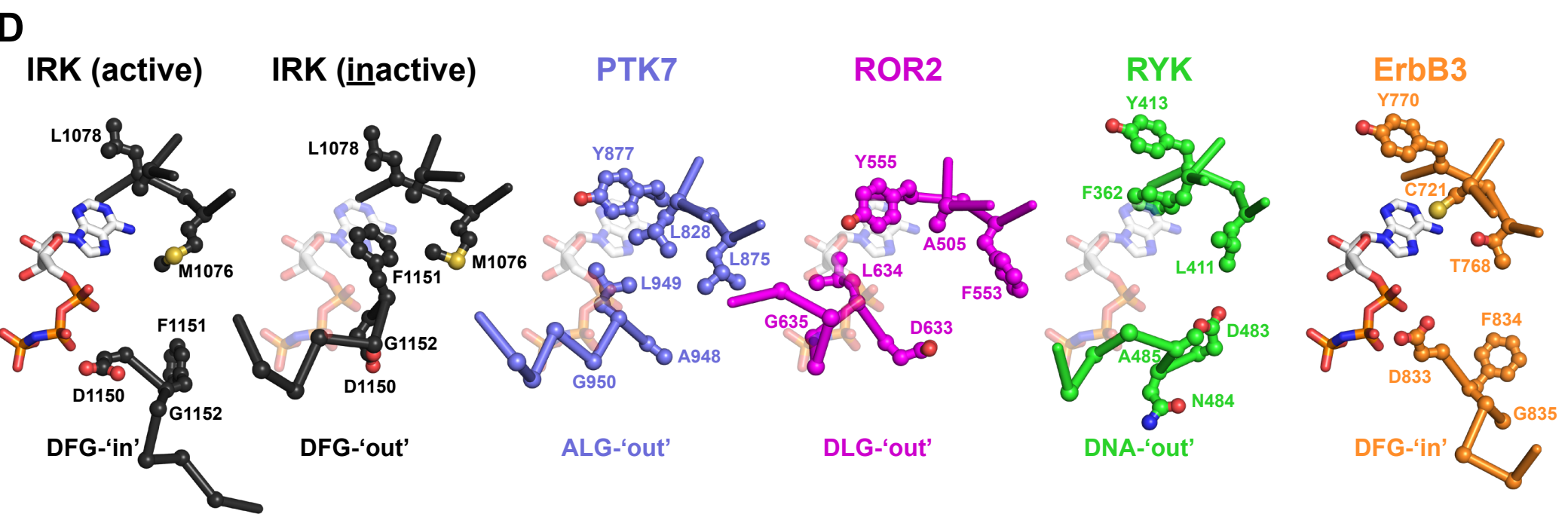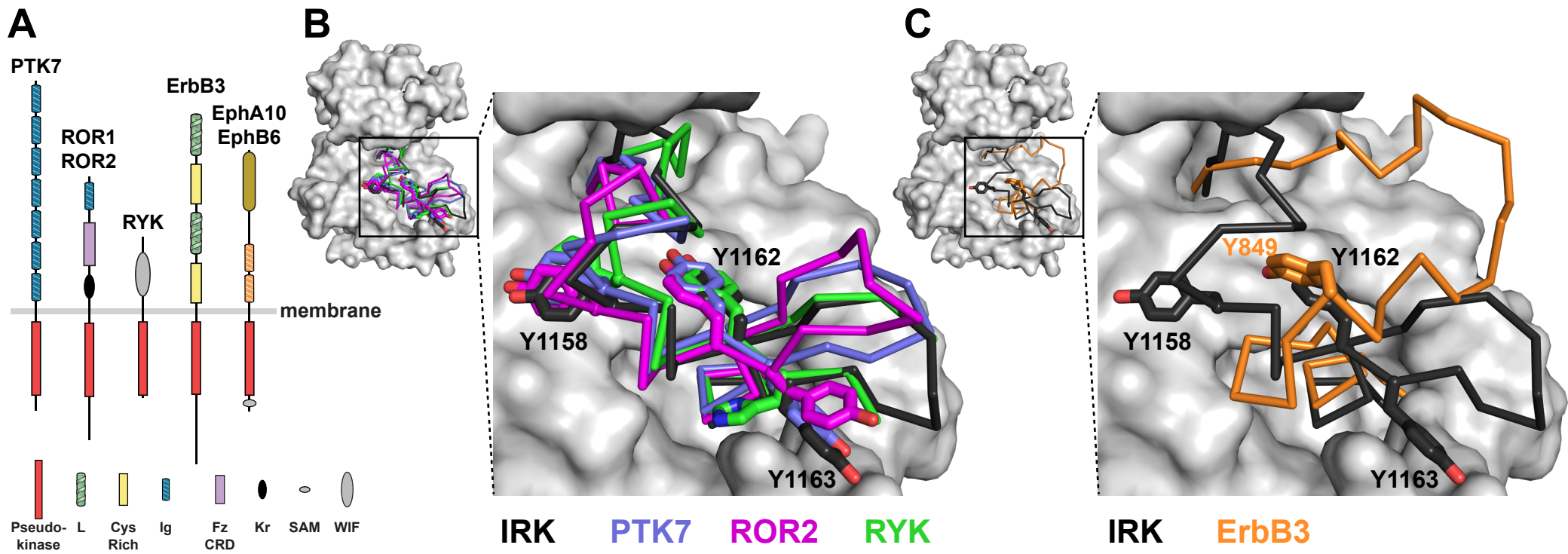
Xie, T., Lim, S.M., Westover, K.D., Dodge, M.E., Ercan, D., Ficarro, S.B., Udayakumar, D., Gurbani, D., Tae, H.S., Riddle, S.M., et al. (2014). Pharmacological targeting of the pseudokinase Her3. Nat. Chem. Biol. *10*, 1006-1012.
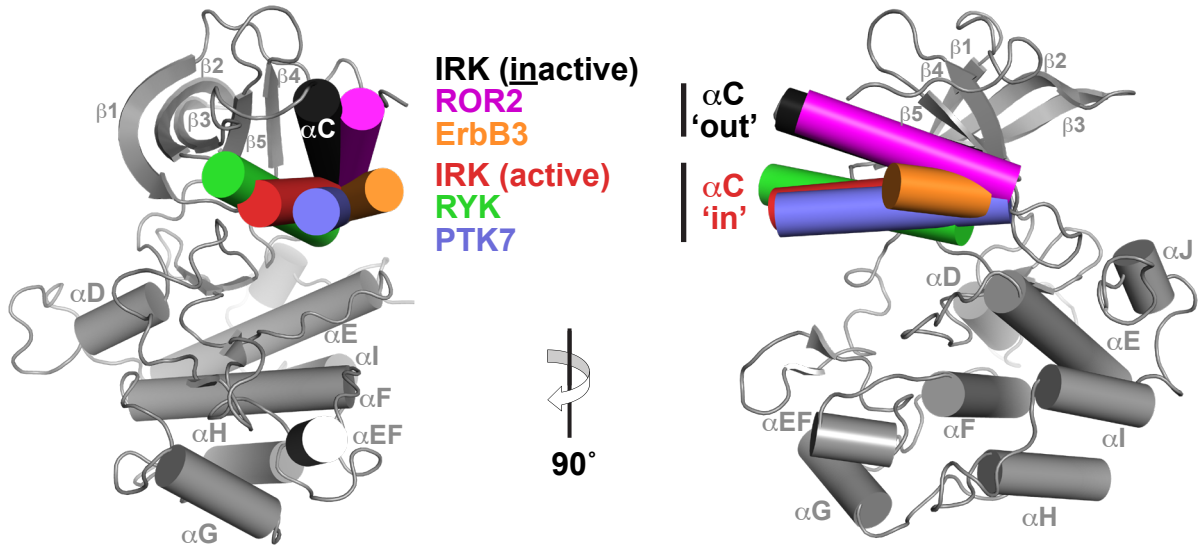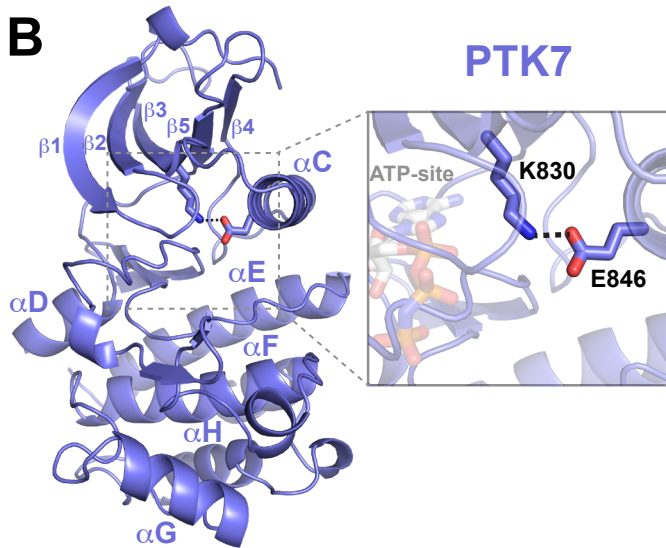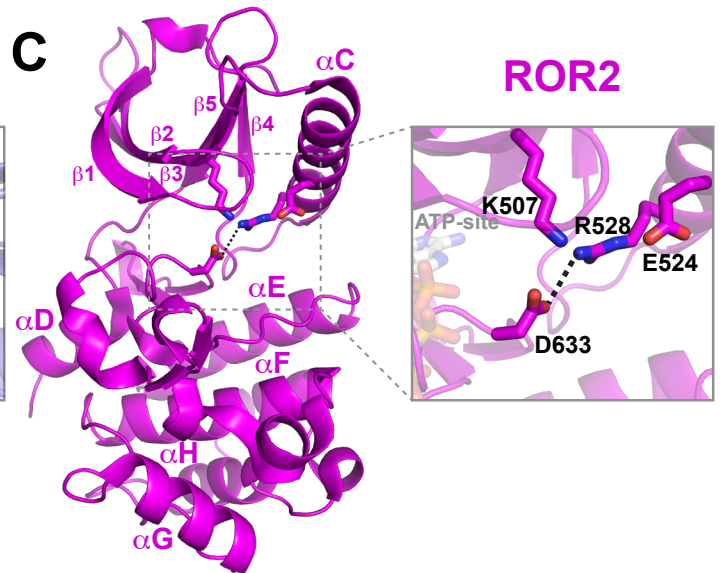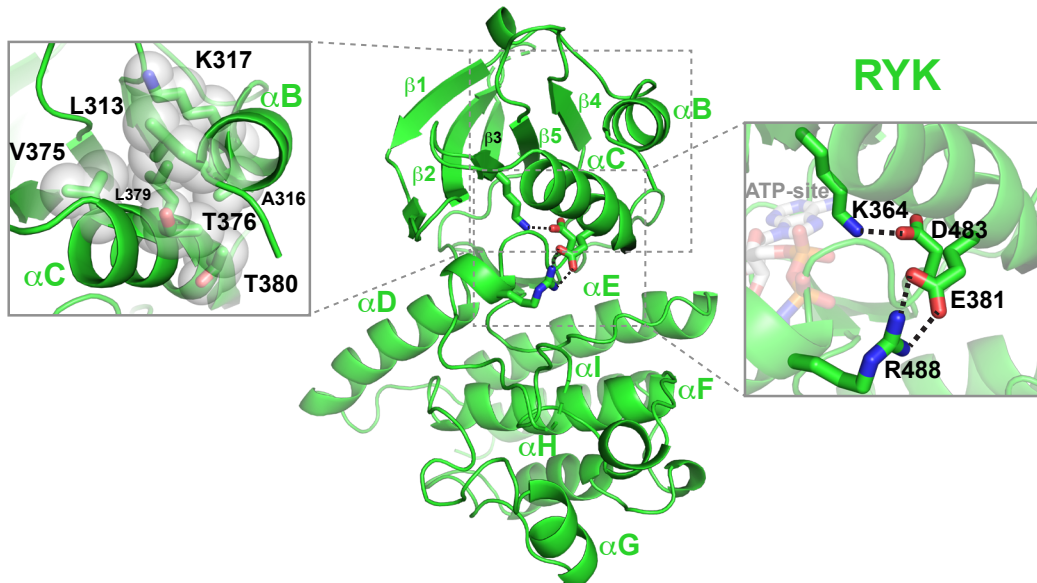
Yamaguchi, T., Yanagisawa, K., Sugiyama, R., Hosono, Y., Shimada, Y., Arima, C., Kato, S., Tomida, S., Suzuki, M., Osada, H., et al. (2012). NKX2-1/TITF1/TTF-1-induced ROR1 is required to sustain EGFR survival signaling in lung adenocarcinoma. Cancer Cell *21*, 348-361.
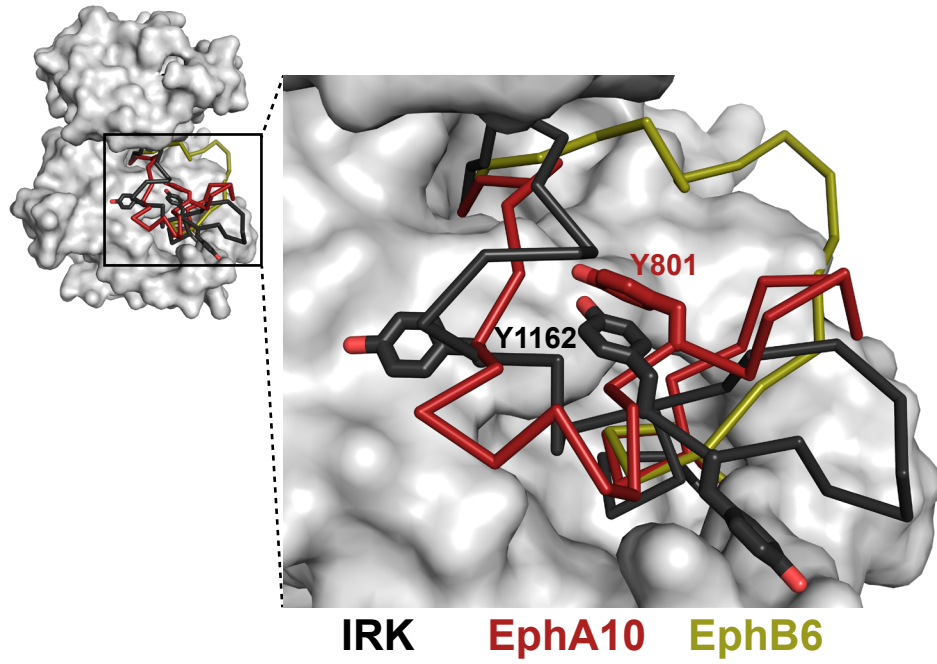
Zeqiraj, E., Filippi, B.M., Goldie, S., Navratilova, I., Boudeau, J., Deak, M., Alessi, D.R., and van Aalten, D.M. (2009). ATP and MO25alpha regulate the conformational state of the STRADalpha pseudokinase and activation of the LKB1 tumour suppressor. PLoS Biol. *7*, e1000126.

Zeqiraj, E., and van Aalten, D.M. (2010). Pseudokinases-remnants of evolution or key allosteric regulators? Curr. Opin. Struct. Biol. *20*, 772-781.

Zhang, S., Zhang, H., Ghia, E.M., Huang, J., Wu, L., Zhang, J., Lam, S., Lei, Y., He, J., Cui, B., et al. (2019). Inhibition of chemotherapy resistant breast cancer stem cells by a ROR1 specific antibody. Proc. Natl. Acad. Sci. U. S. A. *116*, 1370-1377.

A

PTK7

ROR1
ROR2

RYK

ErbB3

EphA10
EphB6

membrane

Pseudo-kinase | L | Cys Rich | Ig | Fz CRD | Kr | SAM | WIF

B

IRK   PTK7   ROR2   RYK

Y1162
Y1158
Y1163

C

IRK   ErbB3

Y849   Y1162
Y1158
Y1163

D

IRK (active)
L1078
M1076
D1150
F1151
G1152
DFG-'in'

IRK (inactive)
L1078
F1151
M1076
G1152
D1150
DFG-'out'

PTK7
Y877
L828
L875
L949
A948
G950
ALG-'out'

ROR2
Y555
A505
L634
F553
G635
D633
DLG-'out'

RYK
Y413
F362
L411
D483
A485
N484
DNA-'out'

ErbB3
Y770
C721
T768
F834
D833
G835
DFG-'in'

A

IRK (inactive)
ROR2
ErbB3
IRK (active)
RYK
PTK7

αC 'out'

αC 'in'

B PTK7

ATP-site
K830
E846

C ROR2

ATP-site
K507
R528
E524
D633

D RYK

K317
L313
αB
V375
L379
A316
αC
T376
T380

K364
D483
E381
R488
ATP-site

A — IRK   EphA10   EphB6

B — EphA10 / IRK

EphA10: R774, H775, H-R-G, Y801

IRK: N1137, R1136, D1132, H-R-D, Y1162

C — EphA10 / EphB6

EphA10: Y725, Y723, G790, G788, F789, GFG-'out'

EphB6: F750, T748, R813, L814, G815, RLG-'in'

A

IRK# β1 β2 β3 αC β4 β5 αD αE β7 β8 β10 β11 αEF αF αG αH αI

980 — — — — — — — — — — — — — — — — — 1280

β5/αD Hinge   HRD   A-loop

Peptides Recovered

% Exchange at 1 min: 100, 80, 60, 40, 20, 0

IRK

YxxxYY

% Exchange

Exchange time (IRK):
- 10 sec
- 1 min
- 10 min
- 1 hr
- 2 hrs

980   1080   Residue Number   1180   1280

B

β1 β3 β5 β2 β4 αC

β5/αD Hinge

αD αE αI HRD αF

A-loop

αH

αG

C

10 sec

1 min

PTK7
ROR2
RYK
ROR1

10 min

2 hr

980   1080   Residue Number   1180   1280

D

β1 β3 β5 β2 β4 αC

αD αE αI αF

αH

αG

-6σ   -2σ   2σ   6σ

less exchange in pseudokinase   more exchange in pseudokinase

A PTK7, ROR2, RYK, ROR1 — T_M shift (°C) versus 1500 compounds. ROR1 panel labeled GZD824 and Ponatinib.

B Ponatinib, Ror1 ΔT_M = 4.1°C; GZD824, Ror1 ΔT_M = 6.0°C

C ROR1 T_M shift (°C) versus [GZD824] (M)

D Ponatinib and GZD824 immunoblots, Temp 42–60°C, Inhibitor − +, HA-ROR1, β-tubulin

E Relative band intensity versus Temperature (°C); Ponatinib (10μM), GZD824 (10μM), Control

G-rich loop

β1   β2   β3   αB   αC

```
IRK     ITLLRELGQGSFGMVYEGNA-RDIIK-GEAETRVAVKTVNESAS--LRERIEFLNEASVMKGFTCH-HVVR    1061
PTK7    LQPITTLGKSEFGEVFLAKA-QGL-EEGVAETLVLVKSLQSKDE---QQQLDFRRELEMFGKL-NHANVVR    860
ROR1    VRFMEELGECAFGKIYKGHL-YLPG-MDHA-QLVAIKTLKDYNN--PQQWTEFQQEASLMAEL-HHPNIVC    537
ROR2    VRFMEELGEDRFGKVYKGHL-FGPAPGEQT-QAVAIKTLKDKAE--GPLREEFRHEAMLRARL-QHPNVVC    538
RYK     ITLKDVLQEGTFGRIFHGIL-IDEKDPNK-EKQAFVKTVKDQAS--EIQVTMMLTESCKLRGL-HHRNLLP    395
EphA10  VTLERSLGGGRFGELCCGCL-QLP-GRQEL--LVAVHMLRDSAS--DSQRLGFLAEALTLGQF-DHSHIVR    708
EphB6   IKIEEVIGTGSFGEVRQGRL-QPR-GRREQ--TVAIQALWAGGA--ESLQMTFLGRAAVLGQF-QHPNILR    733
ErbB3   LRKLKVLGSGVFGTVHKGVW-IPEGESIKI--PVCIKVIEDKSG--RQSFQAVTDHMLAIGSL-DHAHIVR    754
EGFR    FKKIKVLGSGAFGTVYKGLW-IPEGEKVKI--PVAIKELREATS--PKANKEILDEAYVMASV-DNPHVCR    752
PKA     FDRIKTLGTGSFGRVMLVKH-KESG------NHYAMKILDKQKVVKLKQIEHTLNEKRILQAV-NFPFLVK    105
```

β4   β5   **gate keeper**   αD   αE

```
IRK     LLGV-VSKGQPTLVVMELMAHGDLKSYLRSLRP------EAENN-PGRPPPTLQEMIQMAAEIADGMAYLN   1124
PTK7    LLGL-CREAEPHYMVLEYVDLGDLKQFLRISK-------SKDEK-LKSQPLSTKQKVALCTQVALGMEHLS    922
ROR1    LLGA-VTQEQPVCMLFEYINQGDLHEFLIMRSPHSDVGCSSDEDGTVKSSLDHGDFLHIAIQIAAGMEYLS    607
ROR2    LLGV-VTKDQPLSMIFSYCSHGDLHEFLVMRSPHSDVG-STDDDRTVKSALEPPDFVHLVAQIAAGMEYLS    607
RYK     ITHVCIEEGEKPMVILPYMNWGNLKLFLRQCK-----LVEANNP----QAISQQDLVHMAIQIACGMSYLA    457
EphA10  LEGV-VTRGSTLMIVTEYMSHGALDGFLRRHEG---------------QLVAGQLMGLLPGLASAMKYLS    762
EphB6   LEGV-VTKSRPLMVITEFMELGPLDSFLRQREG---------------QFSSLQLVAMQRGVAAAMQYLS    787
ErbB3   LLG--LCPGSSLQLVTQYLPLGSLLDHVRQHRG---------------ALGPQLLLNWGVQIAKGMYLE    807
EGFR    LLGICLT--STVQLITQLMPFGCLLDYVREHKD---------------NIGSQYLLNWCVQIAKGMNYLE    805
PKA     LEFS-FKDNSNLYMVMEYVAGGEMFSHLRRIG---------------RFSEPHARFYAAQIVLTFEYLH    158
```

HRD motif   **DFG motif**   **YxxxYY motif**

β6   β7   β8   β9   β10   β11   αEF   αF

```
IRK     AKKFVHRDLAARNCMVAHDFTVKIGDFGMTRDIYETDYYRKGGKGLLPVRWMAPESLKDGVFTTSSDMWSF   1195
PTK7    NNRFVHKDLAARNCLVSAQRQVKVSALGLSKDVYNSEYYHFRQ-AWVPLRWMSPEAILEGDFSTKSDVWAF    992
ROR1    SHFFVHKDLAARNILIGEQLHVKISDLGLSREIYSADYYRVQSKSLLPIRWMPPEAIMYGKFSSDSDIWSF    678
ROR2    SHHVVHKDLATRNVLVYDKLNVKISDLGLFREVYAADYYKLLGNSLLPIRWMAPEAIMYGKFSIDSDIWSY    678
RYK     RREVIHKCLDLAARNCVIDDTLQVKITDNALSRDLFPMDYHCLGDNENRPVRWMALESLVNNEFSSASDVWAF    528
EphA10  EMGYVHRGLAARHVLVSSDLVCKISGFGRGPRDRSEAVYTTMS-GRSPALWAAPETLQFGHFSSASDVWSF    832
EphB6   SFAFVHRSLSAHSVLVNSHLVCKVARLGHSPQGPSC----------LLRWAAPEVIAHGKHTTSSDVWSF    847
ErbB3   EHGMVHRNLAARNVLLKSPSQVQVADFGVADLLPPDDKQLLYSEAKTPIKWMALESIHFGKYTHQSDVWSY    878
EGFR    DRRLVHRDLAARNVLVKTPQHVKITDFGLAKLLGAEEKEYHAEGGKVPIKWMALESILHRIYTHQSDVWSY    876
PKA     SLDLIYRDLKPENLLIDQQGYIQVTDFGFAKRVKGRTWTLCGTP---EYLAPEIILSKGYNKAVDWWAL    224
```

Catalytic loop   **Activation loop**

αF   αG   αH   αI

```
IRK     GVVLWEITSLAEQPYQGLSNEQVLKFVMDGG-YLDQPDNCPERVTDLMRMCWQFNPKMRPTFLEIVNLL    1263
PTK7    GVLMWEVFTHGEMPHGGQADDEVLADLQAGKARLPQPEGCPSKLYRLMQRCWALSPKDRPSFSEIASAL    1061
ROR1    GVVLWEIFSFGLQPYYGFSNQEVIEMVRKRQ-LLPCSEDCPPRMYSLMTECWNEIPSRRPRFKDIHVRL    746
ROR2    GVVLWEVFSYGLQPYCGYSNQDVVEMIRNRQ-VLPCPDDCPAWVYALMIECWNEFPSRRPRFKDIHSRL    746
RYK     GVTLWELMTLGQTPYVDIDPFEMAAYLKDGY-RIAQPINCPDELFAVMACCWALDPEERPKFQQLVQCL    596
EphA10  GIIMWEVMAFGERPYWDMSGQDVIKAVEDGF-RLPPPRNCPNLLHRLMLDCWQKDPGERPRFSQIHSIL    900
EphB6   GILMWEVMSYGERPYWDMSEQEVLNAIEQEF-RLPPPPGCPPGLHLLMLDTWQKDRARRPHFDQLVAAF    915
ErbB3   GVTVWELMTFGAEPYAGLRLAEVPDLLEKGE-RLAQPQICTIDVYMVMVKCWMIDENIRPTFKELANEF    946
EGFR    GVTVWELMTFGSKPYDGIPASEISSILEKGE-RLPQPPICTIDVYMIMVKCWMIDADSRPKFRELIIEF    944
PKA     GVLIYE-MAAGYPPFFADQPIQIYEKIVSGK--VRFPSHFSSDLKDLLRNLLQVDLTKRFGNLKNGVND    290
```
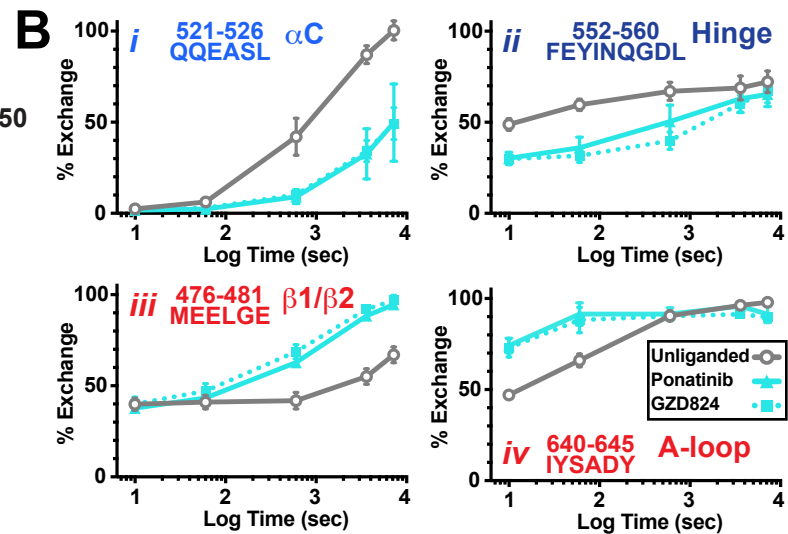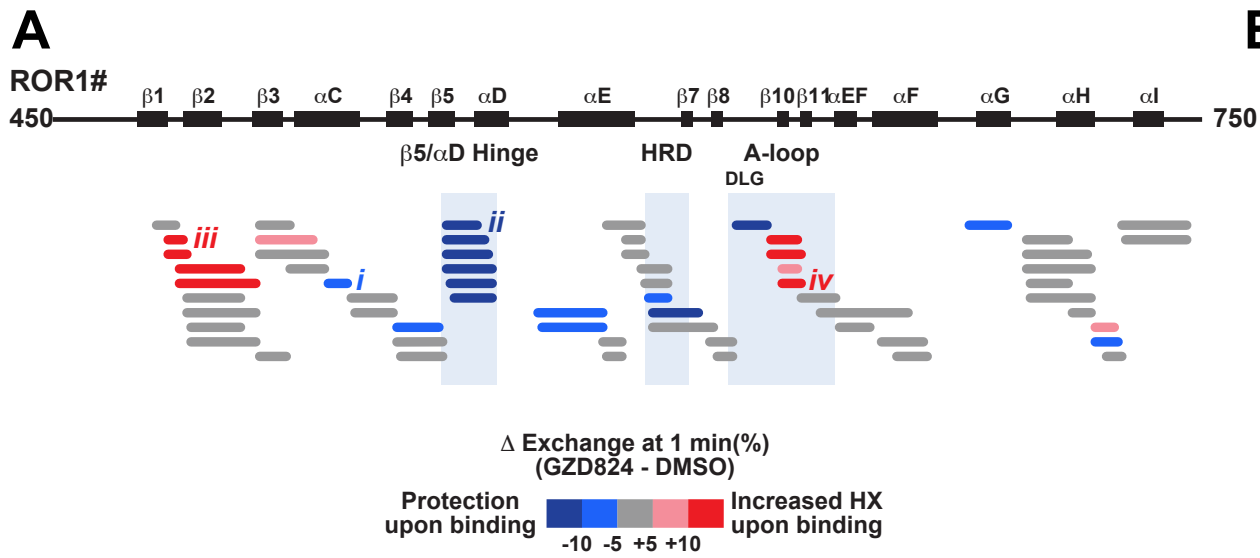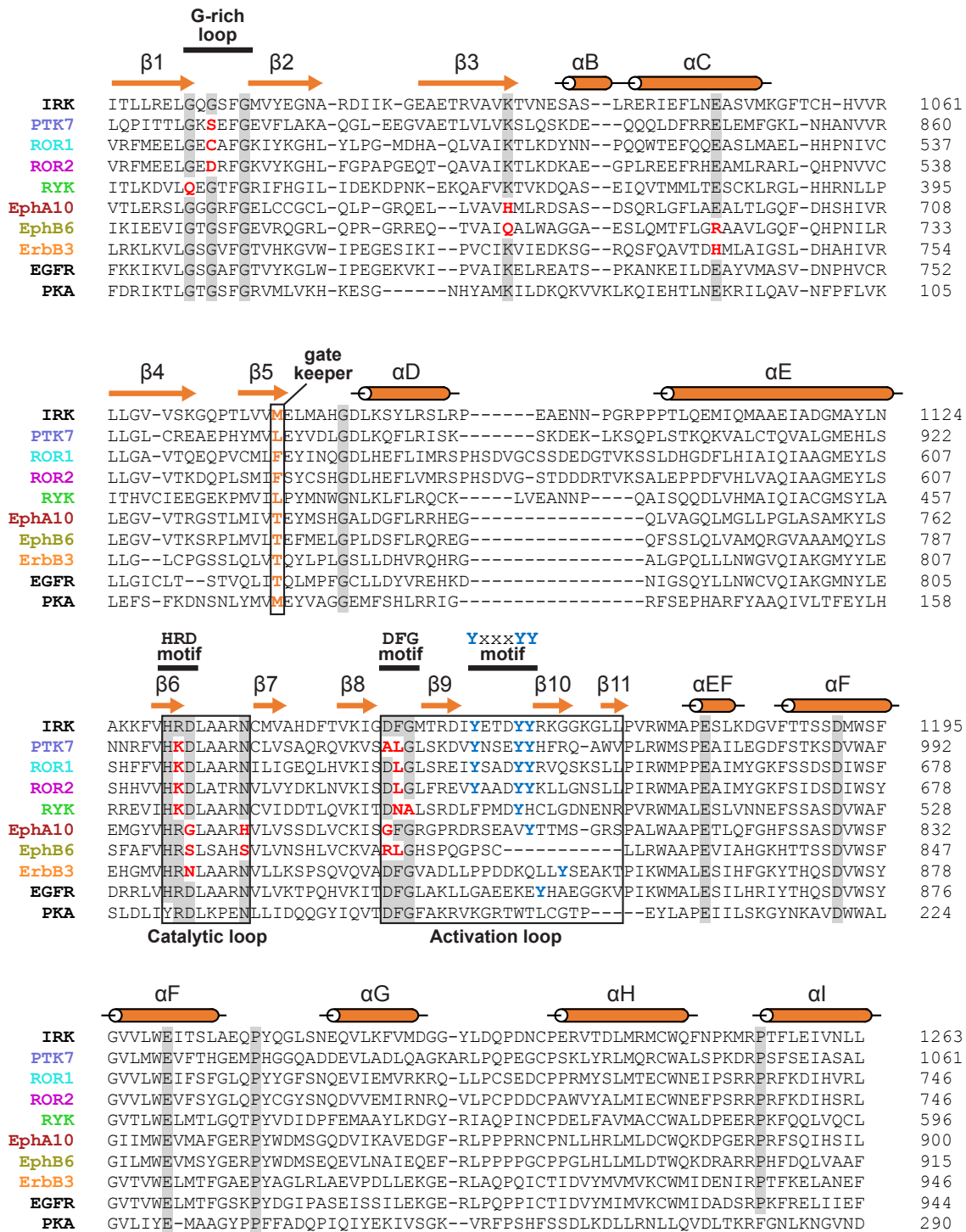
Figure S1 – Related to Figure 1.
Amino acid sequence alignment of RTK pseudokinase domains alongside IRK, EGFR, and protein kinase A (PKA)

Highly conserved residues across all kinases/pseudokinases are boxed in grey; sequence variations in pseudokinases for key conserved residues are in bold red text. Secondary structure elements are noted, as are the catalytic and activation loop regions as well as the G-rich loop, HRD, and DFG motifs. Putative regulatory activation-loop tyrosine residues (in the YxxxYY motif) are in bold blue text, and the gatekeeper residue is in orange text.
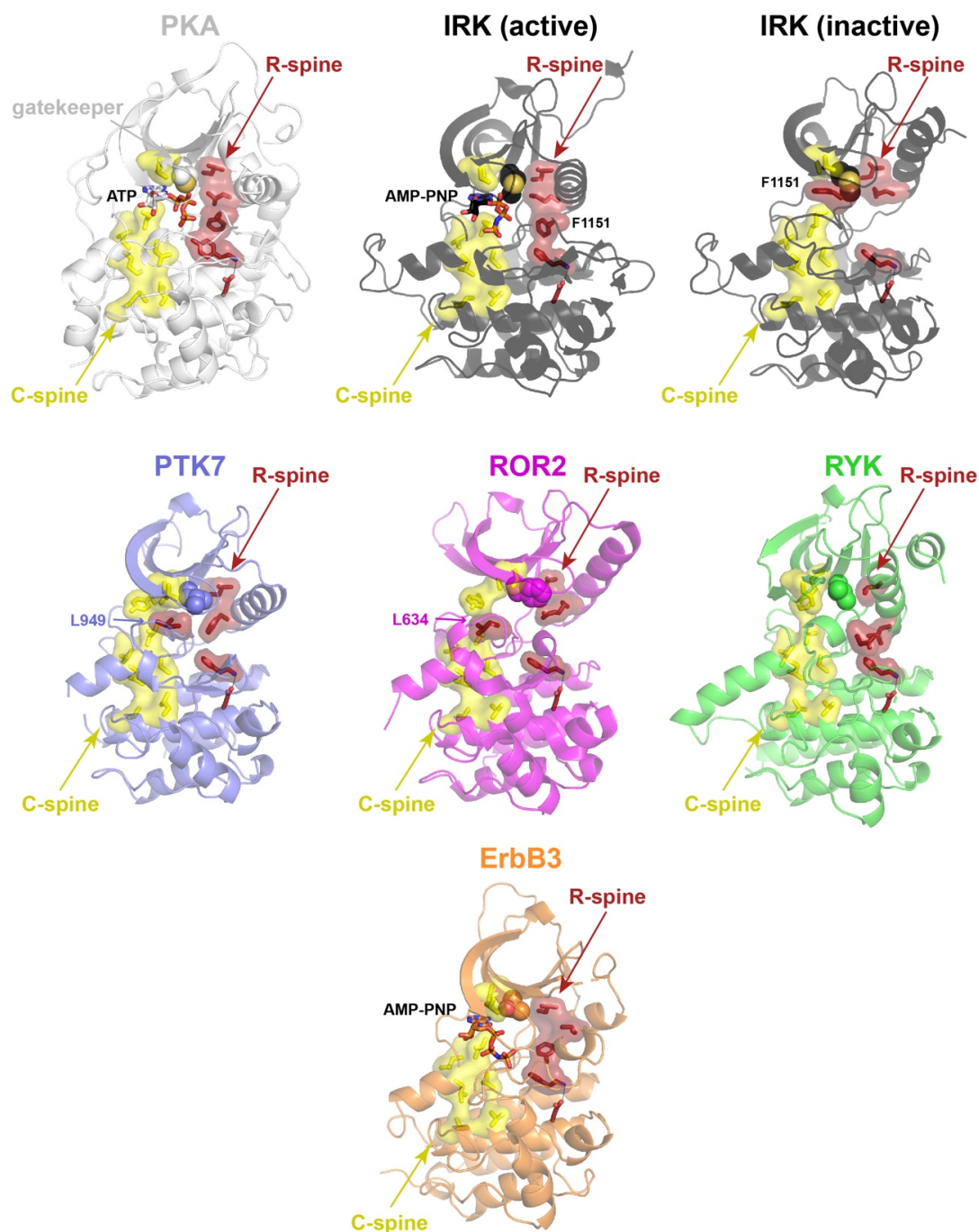
1

Figure S2 – Related to Figure 2.
Comparison of hydrophobic spines in the RTK pseudokinases
Top row: Cartoon representation of the catalytically active kinases PKA (white; PDB: 1ATP) and IRK (black) in its active (PDB: 1IR3) and inactive (PDB: 1IRK) conformations. Residues comprising the catalytic spine (C-spine) and the regulatory spine (R-spine) for each domain are shown in surface representation and colored yellow or red, respectively. Both are complete in the active kinases – with the C-spine completed by the adenine ring of ATP. In inactive IRK, F1151 of the DFG motif instead occupies the adenine ring position in the C-spine. Upon activation loop phosphorylation and ligation of the ATP-binding site, F1151 flips from this position towards the αC helix to complete the R-spine. The 'gatekeeper' residue (homologous to threonine 315 in ABL) is shown for each domain in sphere representation, and ATP or AMP-PNP is also shown where bound.

2

Middle row: Pseudokinase domains from PTK7 (slate blue), ROR2 (magenta; PDB: 4GT4), and RYK (green). The C-spine is completed in each case by aromatic side-chains that take the place of an ATP ligand. In PTK7 and ROR2, the leucine that replaces the DFG phenylalanine (L949 in PTK7's 'ALG' motif, and L634 in ROR2's 'DLG' motif) abuts the C-spine, but does not contribute to its completion like F1151 does in inactive IRK. Although these residues do not contribute to C-spine completion, they also do not contribute to the R-spine – which is broken in both cases. In RYK, the C-spine is complete, and the R-spine is broken because it lacks an equivalent hydrophobic residue to the DFG phenylalanine (replaced by N of DNA, which is in displaced from the spine.

Bottom: The C- and R-spines of ErbB3 (orange; PDB: 4RIW) are shown, both complete, with an arrangement that resembles active kinases.
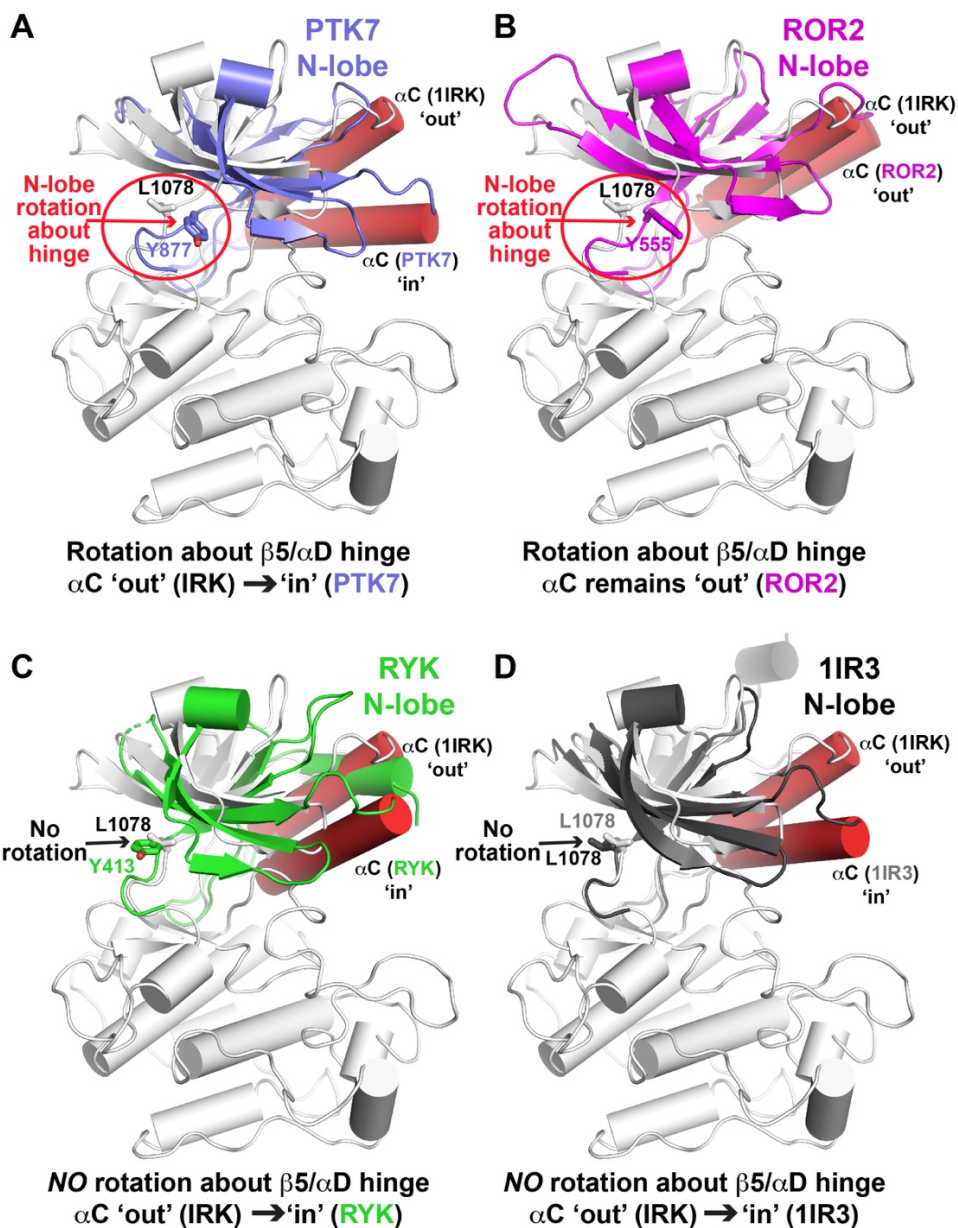
Figure S3 – Related to Figure 3.
Rotation of the N-lobe and position of the αC helix in the RTK pseudokinases
The N-lobes of the pseudokinase domains from (**A**): PTK7 (slate blue), (**B**): ROR2 (magenta),
(**C**): RYK (green), and (**D**): active IRK (black; PBD: 1IR3) were individually overlaid on <u>in</u>active IRK
(white; PDB: 1IRK) based on superimpositions of the kinase C-lobes – to inspect differences in N-lobe
orientation as a result of rotation about the β5/αD hinge. The C-lobe of only inactive IRK is
represented (for clarity). Helix αC is colored red in each domain.

In (**A**), the αC helix is clearly 'out' for inactive IRK and 'in' for PTK7. In addition, the entire N-lobe
has undergone a rotation about the β5/αD hinge (marked in red) that also causes Y877 (marked) to
project into the ATP-binding site (which it occludes) – whereas the corresponding IRK residue (L1078)
projects away from the ATP-binding site. In (**B**), αC is 'out' for both ROR2 and inactive IRK, but ROR2
also displays the N-lobe rotation about the β5/αD hinge seen for PTK7 – in this case causing the
Y555 side-chain of ROR2 to occlude the ATP-binding site. In (**C**), RYK displays an αC 'in'
conformation (like PTK7), but its N-lobe has not undergone rotation about the β5/αD hinge, so the
Y413 side-chain aligns with IRK L1078 and projects away from the ATP-binding site. In (**D**), active
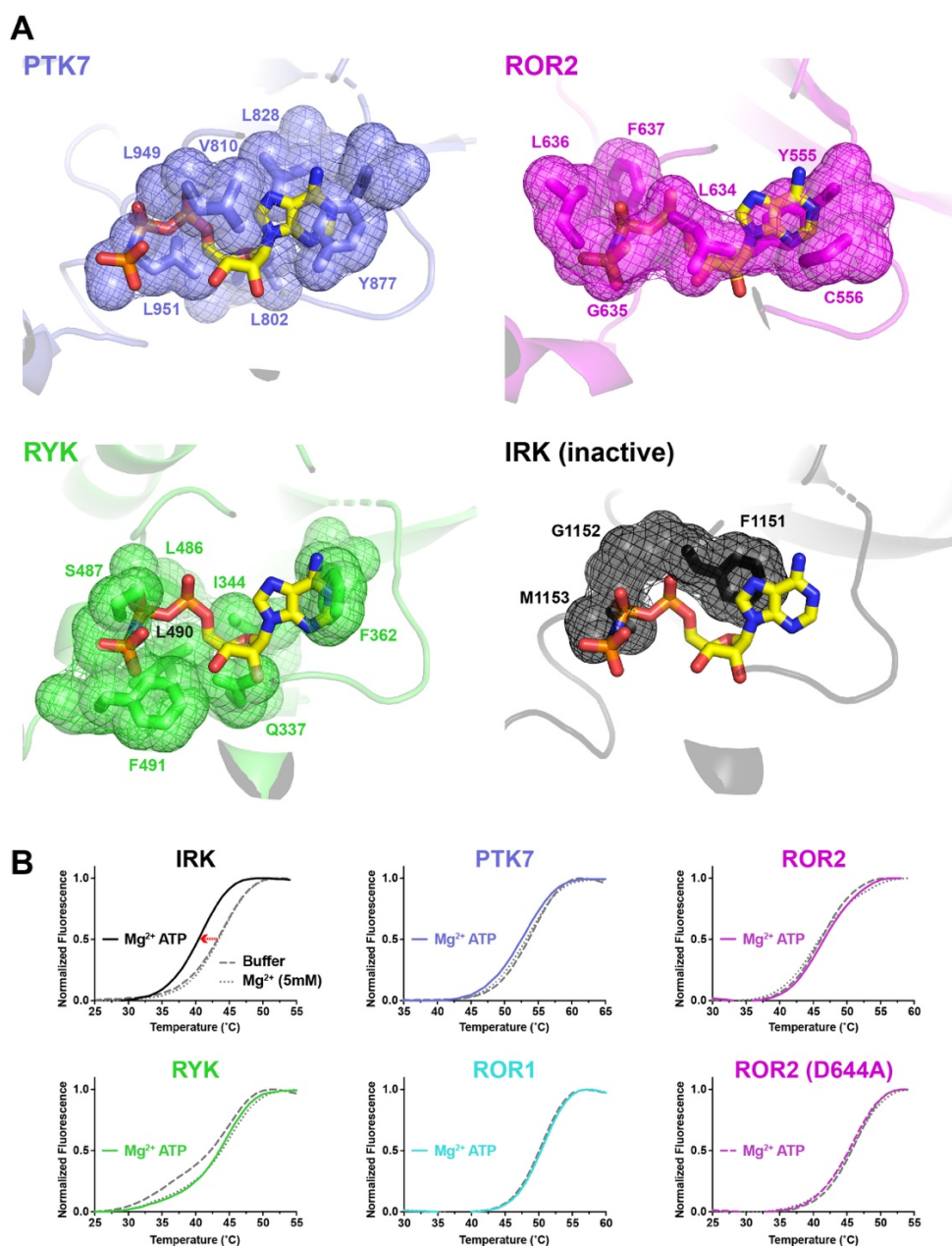and inactive IRK are overlaid – with no N-lobe rotation, but a clear αC displacement.

Figure S4 – Related to Figure 4.
Occlusion of the nucleotide-binding site prevents ATP-binding in Wnt-binding pseudokinases
(**A**) Detailed structural view of the occluded ATP-binding sites of PTK7 (slate blue), ROR2 (magenta), RYK (green), and inactive IRK (black; PBD: 1IRK). Residues contributing to steric occlusion of the nucleotide-binding site are labelled and shown in both stick representation with a transparent surface and mesh for emphasis, with AMP-PNP placed based on superimposition with active IRK (PDB: 1IR3) – to highlight the degree of occlusion.
(**B**) DSF analysis of the melting temperatures of IRK and the PTK7, ROR2, RYK, and ROR1 pseudokinases in the presence and absence of 5 mM ATP and/or MgCl$_2$. For IRK, the presence of ATP and Mg^{2+} results in a leftward shift ($\Delta T_M \sim 3.5°C$) in the melting curve, indicating decreased IRK stability upon Mg^{2+}-ATP binding. By contrast, the melting curves of PTK7, ROR2, RYK, and ROR1 were unchanged. Mutating the activation loop aspartate in ROR2 to alanine (D644A) – analogous to the IRK D1161A mutation that increases ATP-binding affinity ~20-fold even without phosphorylation (Ablooglu et al., 2001) – had no effect on the ATP-binding properties of ROR2. Curves represent means of three technical replicates.
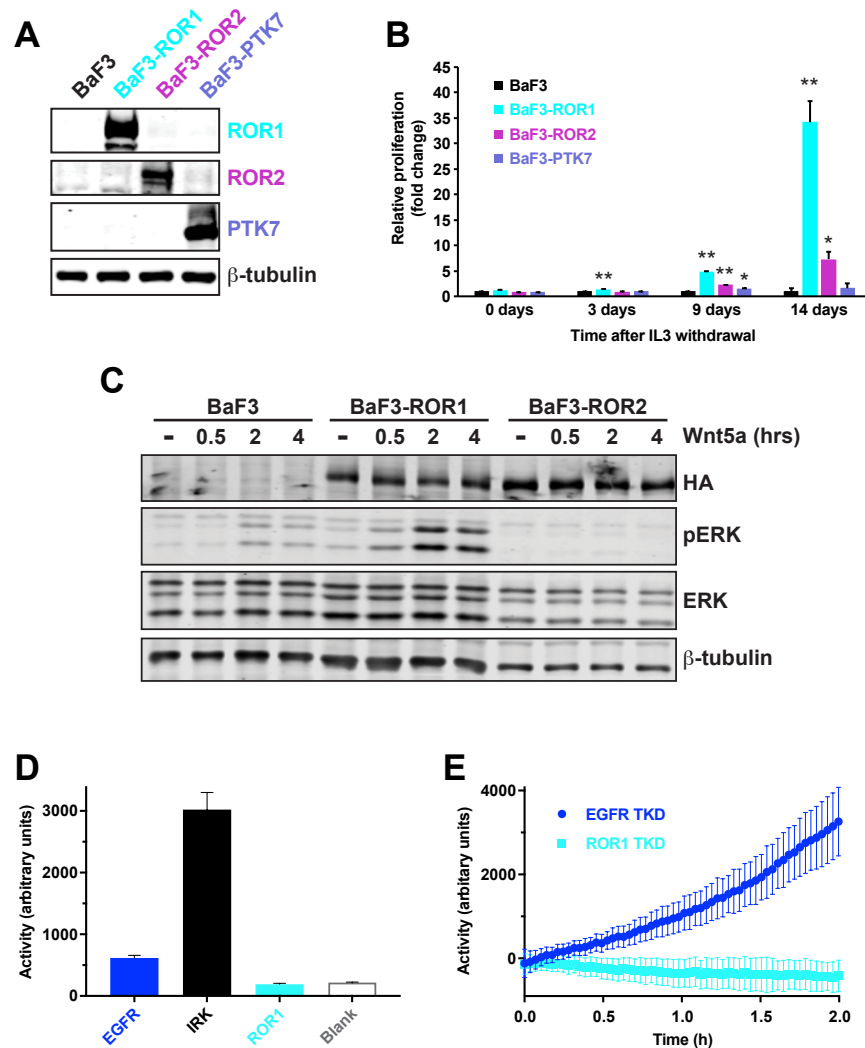
Figure S5 – Related to Figure 5.
Analysis of protein expression and cell survival following stable expression of ROR1, ROR2 and PTK7 in BaF3 cells.
(**A**) BaF3 parental and BaF3-ROR1, BaF3-ROR2 and BaF3-PTK7 stable clones were analyzed for expression of ROR1, ROR2 and PTK7 by Western blotting with the indicated antibodies and β-tubulin as loading control.
(**B**) Ability of BaF3 cells expressing ROR1, ROR2 or PTK7 to proliferate in the absence of IL3 or Wnt5a. Relative cell proliferation at the indicated times was measured using the CellTiter-Glow 2.0 Assay, and expressed as a fold increase over the proliferation seen for parental BaF3 cells. Data are represented as mean ± SD, for 3 biological repeats. ***$p \leq 0.001$; **$p \leq 0.01$; *$p \leq 0.05$.
(**C**) Wnt5a stimulation increases ERK phosphorylation in BaF3-ROR1, but not BaF3-ROR2 cells. Experiments were performed as in Fig. 5C, with 50 ng/ml Wnt5a, and detection of ROR1 and ROR2 protein levels using anti-HA blotting. A representative of three independent experiments is shown.
(**D**) Endpoint in vitro kinase assay, assessing phosphorylation of poly(Glu,Tyr) substrate during a 1 h incubation at room temperature for monomeric wild-type EGFR kinase (k_{cat} approximately 2 min^{-1}), IRK, and ROR1 . See STAR Methods for experimental details. Data are presented as mean ± SD of experimental triplicates.
(**E**) Time courses of in vitro kinase activity towards a sulfonamido-oxine (Sox) chromophore-incorporated fluorescent peptide substrate for 1 μM EGFR wild-type kinase domain (k_{cat} approximately 2 min^{-1}) and 1 μM ROR1 pseudokinase domain. See STAR Methods for experimental details. Data are mean ± SD of experimental triplicates.
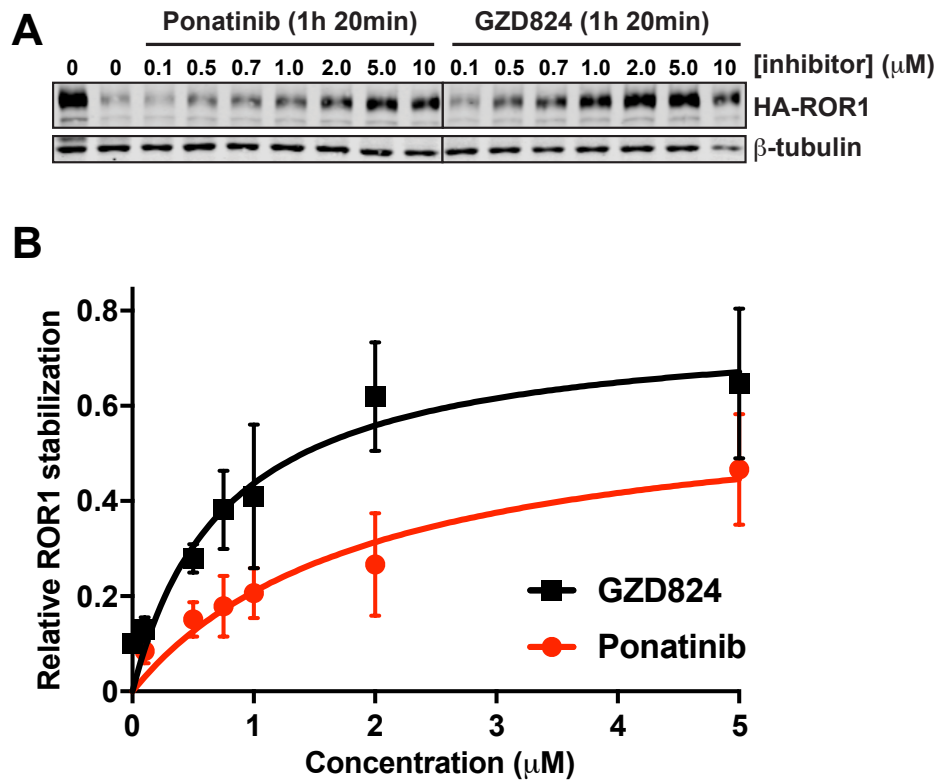
Figure S6 – Related to Figure 6.
CETSA analysis for concentration-dependent binding of ponatinib or GZD824 to ROR1
(**A**) Representative Western blots showing stabilization of ROR1 expressed in BaF3 cells by
increasing doses of ponatinib or GZD824. Cells were incubated at 48˚C as described in STAR
Methods prior to immunoblotting to quantitate remaining non-degraded protein.
(**B**) Quantification of Western blots from (**A**). Band intensities were normalized to the intensity from the
non-treated sample for each experiment. Data are presented as means ± SD, n ≥ 3 independent
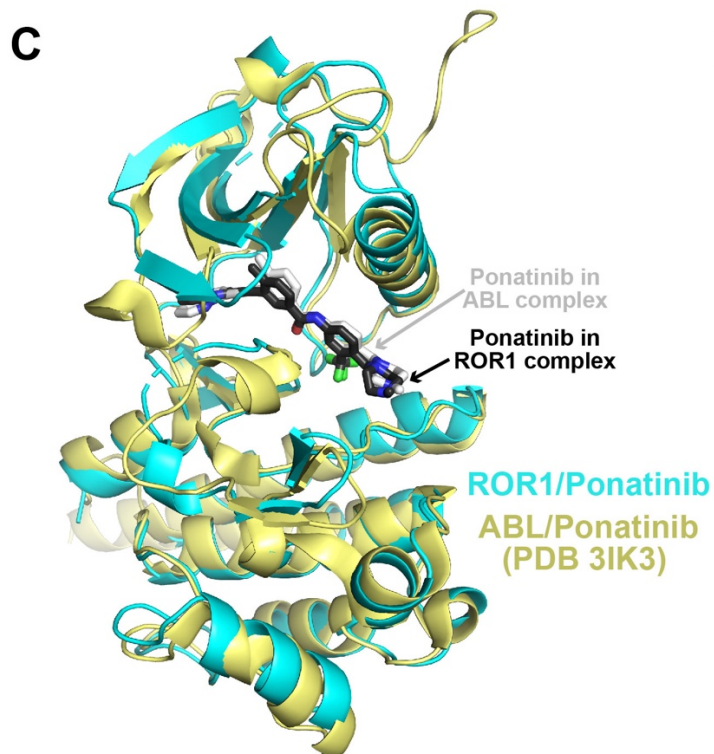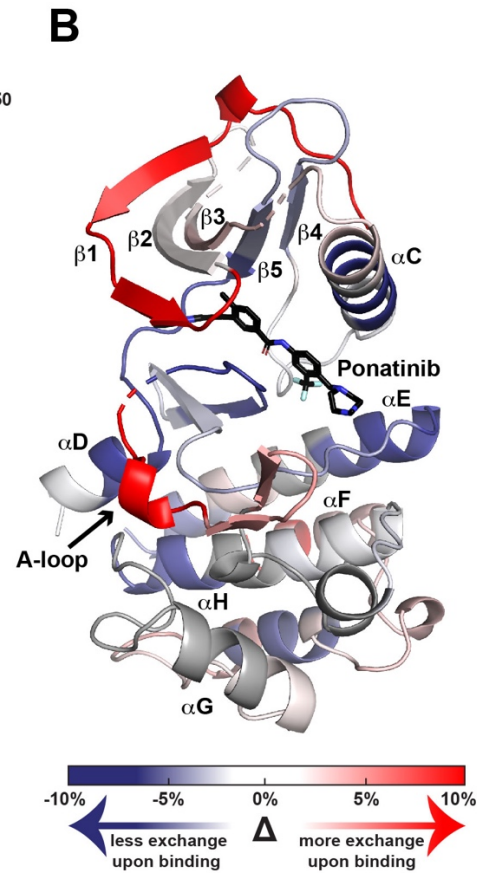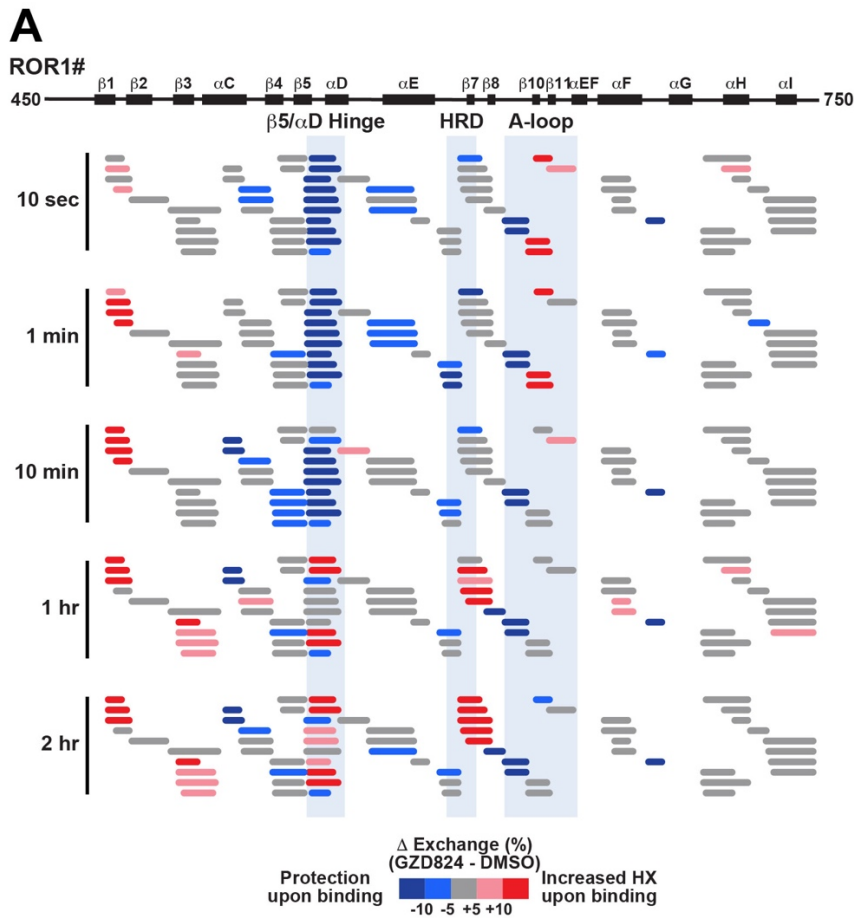experiments (biological repeats).
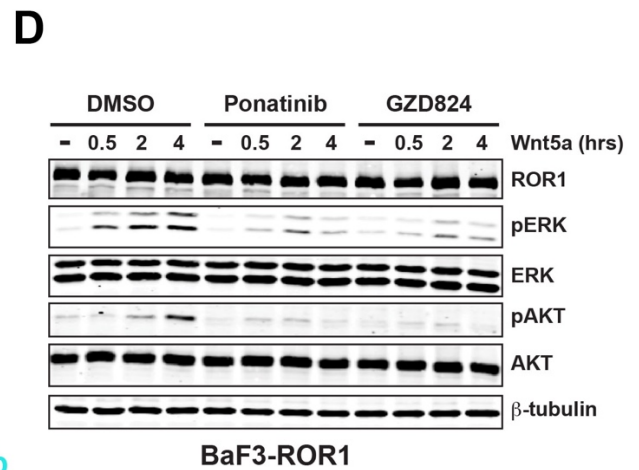
Figure S7 – Related to Figure 7.
Ponatinib/GZD824 is associated with altered ROR1 dynamics and can inhibit Wnt5a signaling
(**A**) Summary of exchange differences observed in the ROR1 pseudokinase in the presence or absence of 50 μM GZD824 as monitored by HDX-MS. Data are shown for all time points. Peptides recovered across each time point are represented by horizontal lines, color coded based on the difference in percent exchange relative to a fully deuterated standard. As shown in the scale at bottom, red represents an HDX increase upon inhibitor binding, and blue represents a reduction in exchange. ROR1 secondary structure is shown at top. Results represent the mean of three biological repeats.
(**B**) HDX results from Fig. S7A (1 min time point) are plotted on the ponatinib-bound ROR1 pseudokinase domain data using the same color scheme as in (**A**), with blue representing less exchange, and red more exchange, upon inhibitor binding.
(**C**) Structural superimposition of the ponatinib-bound ROR1 pseudokinase (cyan) on the ponatinib-bound ABL kinase domain (yellow; PDB 3IK3), with ponatinib shown in black when bound to ROR1 and in white when bound to ABL. Ponatinib docks into the ROR1 pseudokinase domain in virtually the same (type II) orientation as seen with ABL.
(**D**) Adding ponatinib or GZD824 at 1 μM to BaF3 cells expressing full-length ROR1 inhibits the Wnt5a-dependent increases in ERK, AKT, and SRC phosphorylation shown in Fig. 5C. Cells were stimulated with 50 ng/ml Wnt5a for 0, 0.5, 2, or 4 h in the absence or presence of the inhibitors. Cell lysates were then blotted with anti-ROR1 (to assess total ROR1 levels), and with anti-pERK, anti-ERK, anti-pAKT, anti-AKT, and anti-β-tubulin (as a loading control) as described in STAR Methods. Blot is representative of three biological replicates.